ISSN: 2636-8668

Turkish Journal of materials

an international peer-reviewed open access journal

Science Literature
SL PUBLISHING
www.scienceliterature.com

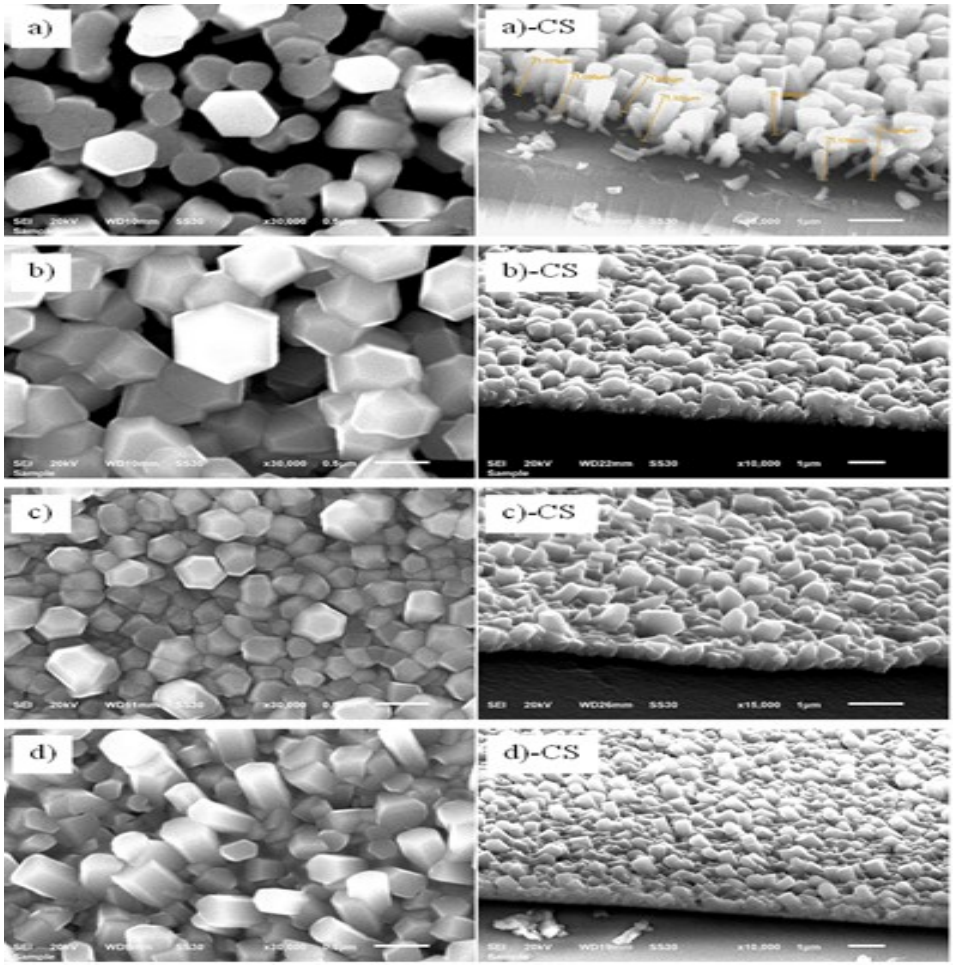

TURKISH JOURNAL OF MATERIALS

VOLUME 1 NO 1

ISSN 2636-8668

2016 July-December Issue

SCIENCE LITERATURE

Kazım Karabekir Work-Center,
F:3/C/196, 50. Year Street,
Lalapaşa Neighborhood,
Yakutiye, Erzurum, Turkey

https://www.scienceliterature.com

01.12.2016

Science Literature

Editorial Article | *Submit Manuscript*

Turkish Journal of Materials

Article preparing template for Turkish Journal of Materials

A.A. One[1,*], A.B. Two[2], A.C. Three[3]

[1]Department Name, Organization Name, City, Country
[2]Department Name, University Name, City, Country
[3]Department Name, University Name, City, Country

Published: 31/12/2016
Turk. J. Mater. Vol: 1 No: 1 Page: I-III (2016) ISSN: XXXX-YYYY
SLOI: http://www.sloi.org/sloi-name-of-this-article
*Correspondence E-mail: journal@scienceliterature.com

ABSTRACT This document gives formatting directives to copy editors and authors preparing papers for publication in the journal. This paper must not be used any other purposes. Authors are encouraged to prepare manuscripts directly using this template. This template demonstrates format requirements for the Journal. The abstract should state briefly the purpose of the research, the principal results and major conclusions. The abstract should not exceed 250 words and should be 10 pt. Authors should be avoided to give references in this section and also, should be avoided non-standard or uncommon abbreviations, but if essential they must be defined at their first mention in the abstract itself.

Keywords: Science Literature; Template; Style; Format.

Cite this article: A.A. One, A.B. Two, A.C. Three. Article preparing template for Turkish Journal of Materials. Turk. J. Mater. 1(1) (2016) I-III.

1. INTRODUCTION

This paper is a template for Copy Editors and Authors. If you are reading a paper or PDF version of this template, please download the file from the Science Literature web site at http://www.scienceliterature.com. Thus, you can use it to prepare your manuscript. In this section, please provide an adequate background with presentation a detailed literature survey about the using materials, techniques and reasons of preferred of related study.

According to the article type, widely scanned literature information should be given in this section.

2. EXPERIMENTAL

The detailed experiment should be given with mark (brand) of using materials and measurement devices. The experiment should be understandable and can be repeated easily.

2.1. Procedures for Preparing Submission

A simple way to comply with the formatting requirements of journal is to use this paper and simply type your manuscript into it.

The template is used to format your paper and style the text. All margins, column widths, line spaces, and text fonts are prescribed; please do not alter them. Your paper is one part of the entire proceedings, not an independent document. Please do not revise any of the current designations. Paper should be orderly prepared like sections;

1. INTRODUCTION
2. EXPERIMENTAL
3. RESULTS
4. CONCLUSION

Appendix (Optional)
Acknowledgement (Optional)
References
Biographies (Optional)
Figure(s) with Caption(s) (Optional)
Table(s) with Caption(s) (Optional)

3. RESULTS

The obtaining results, graphs and tables if there are, should be expressed in this section clearly. The subject can be discussed with the similar studies by giving references.

3.1. Page Format

Your paper should use a page size suitable to A4 paper which is 210mm wide and 297mm long. The margins are set as follows: top= 1.5 cm, bottom= 1.5 cm, right=1.75 cm, left = 2.0 cm. Your paper should be in two column format with a space of 0.7 cm between columns.

3.2. Text Font

The entire document should be prepared in Times New Roman font size 10 pt. Paper title should be regular font size 22 pt, centered, bold, and not all with upper case. Author names should be centered, regular font size 10 pt. Affiliations should be regular font size 8 pt and italic. Email address of corresponding author should be centered, font size 8 pt. More than 3 levels of headings should not be used. Level 1 headings should be left-justified, bold, numbered using Arabic numerals, regular font size 10 pt. The all letter of each title capitalized. Level 2, 3 and more headings should be left-justified, italic, numbered using Arabic numerals, regular font size 10 pt. The first letters of each title word capitalized and then lowercased. A line should be given before the each title.

3.3. Equations and Units

Equations should be centered with equation numbers set flush right as in Equ. (1). Formatting for MathType, use the Times + Symbol 11. Use either SI (MKS) or CGS as primary units. As a common mistake, please use (arb. uni.) for abbreviation of “arbitrary units”, not use (a.u.) because of the “atomic unit”.

$$\varphi_{b0} = \frac{kT}{q} \ln\left(\frac{AAT^2}{I_0}\right) \qquad (1)$$

3.4. Tables

For table title, table head, and table text should be provided. Tables and figures can be placed on separate pages at the back of the manuscript if it is necessary. Table body should be centered and in 10 pt Regular font.

Table 1. Publication number in 2013 as an example.

Date	Publications (in 2013)		
	Articles	Journals	Books
1. Half	1234	4	5
2. Half	987	7	6
3. Half	890	9	6
4. Half	566	9	6

3.5. Figures

One Figure or Graph, each with a title, can be placed apart from the article text in the separate page if it is necessary. Figures should be numbered using Arabic numerals in the text. Figures grouped together should have similar dimensions and be labeled "a, b, c", etc. The colorful and black-white images should be imported at a minimum of 300 dots per inch (dpi). Examples; ....in Figure 1, Figure 2(a) shows….., ….from Figure 2(a-d).

3.6. Figure Captions

Figures should be numbered using Arabic numerals. Figure captions should be in 10 pt. Figure captions should be centered below the related figure. A caption should comprise a brief title.

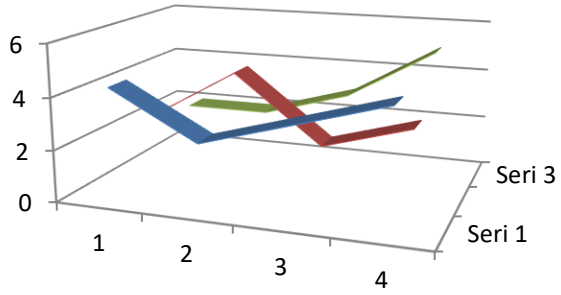

Fig. 1. An example figure for preparing manuscript for a journal of Science Literature.

3.7. Table captions

Table heads should appear above the tables and tables should be numbered using Arabic numerals. Table title should be centered and in 10 pt. Captions with table numbers should be placed above the related tables, as shown in Table 1.

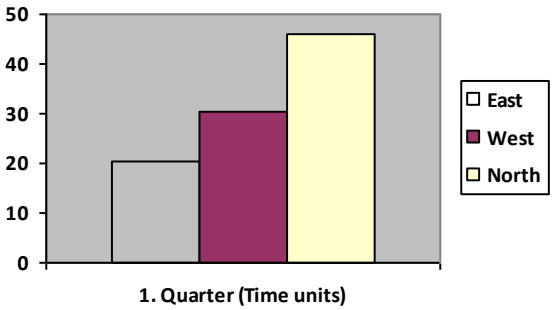

Fig. 2. Graph example. (a) Abcxyz (b) Xyzabc (c) Abcabc (d) Xyzxyz

3.8. References Formats

All reference items should be in 10 pt font. Number the reference items consecutively in square brackets as in [1]. When referring to a reference item, please simply use the reference number, as in [2]. Indicate references by number(s) in square brackets in line with the text. The actual authors can be referred to, but the reference number(s) must always be given.

Example: As demonstrated multiple references [1,4] or [3,6-9]. “Wang and Demir [11] or Brown *et al.* [12]…obtained a similar result.”

4. CONCLUSION

Please include a brief summary of the possible implications of your study in the conclusion section. Although a conclusion may review the main points of the manuscript, please do not replicate the abstract or another part from the text as the conclusion.

Appendix

Appendixes, if needed, appear before the acknowledgment. Please not use number for the heading of this section.

Acknowledgement

Please not use number for the heading of the Acknowledgments section. Acknowledgement example; The authors would like to thank for the contributions of Prof. Dr. Abc Xyz and/or This work was supported by the Abc University Project No: 23232323434-2011.

References

[1] A.A. One, A.B. Two, A.C. Three. Journal citation style: Title of article. J. Sci. Lit. 1(4) (2013) 1-3.
[2] X.A. Four, Y.B. Five, Z.C. Six. Journal citation style: Title of article. J. Sci. Lit. (In Press).
[3] A.A. One, A.B. Two, A.C. Three. Book citation style: Title of book. Science Literature Publishing (2. Ed) (1968) 11-33.
[4] A.A. One, A.B. Two, A.C. Three. Thesis citation style: Title of thesis. Xyz Univ. (2015) 21-23.
[5] A.A. One, A.B. Two, A.C. Three. E-book citation style: Title of e-book. Science Literature Publishing (1. Ed) (2014) 1231-1257.

Biographies (Optional for each journal)

A technical biography for each author may be included. It should begin with the author's full name as bold. A photograph should also be included for each author. The photo should be 2.5 centimeters wide by 3.0 centimeters high. The head and the photo should be flush with the left margin. The space required for each biographies. The following is an example of the text of a technical biography:

Biographies

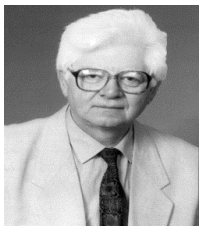

Oktay Sinanoğlu (write your full name) was born on February 25, 1935 in Bari, Italy where his father served as a consul general. In 1939 by the commence of World War II, the family returned to Turkey. In 1953, he attended the high school "TED Yenişehir Lisesi" in Ankara, and after graduating won a scholarship for education of chemistry in the USA. In 1956, he graduated from Berkeley in chemical engineering with the highest rank. In only eight months, he graduated from MIT in1957 with the highest degree. In two years, he finished his doctorate at the University of California at Berkeley. In 1960, Sinanoğlu started working as associate professor at Yale University. He theorized the "Many-Electron Theory of Atoms and Molecules" in1962 by solving a mathematical theorem that had been unsolved for 50 years. The same year, he earned the "Alfred Sloan" prize. As appointed professor in1963 at the age of only 28, he became the youngest person in the past century at Yale to attain the status as a full professor. He got his second life-long chair in Yale in Molecular Biology.

Science Literature

Editorial Letter | *Submit Manuscript*

Turkish Journal of Materials

Developments in Materials Science and Contribution to Science

M.F. Keskenler

Department of Turkish Journal of Materials, Science Literature

Published: 31/12/2016

Turk. J. Mater. Vol: 1 No: 1 page: IV-V (2016) ISSN: XXXX-YYYY

SLOI: http://www.sloi.org/sloi-name-of-this-article

Correspondence E-mail: mfkeskenler@gmail.com

ABSTRACT In materials science unfolds new discoveries and developments day by day. Studies contribute to innovation. Some of these studies examined in this text. Information has been provided on these work and opinions have been expressed on the benefits of the work.

Keywords: Science Literature; Materials; Science.

Cite this article: M.F. Keskenler. Developments in Materials Science and Contribution to Science. Turk. J. Mater. 1(1) (2016) IV-V.

Physicists have added a new member among the exotic species in the sub-atomic world. These new subatomic particles are known as tetraquarks. In Fermilab, a high-energy particle physics laboratory in the US, DZero researchers have discovered tetraquarks. This phenomenon, described as the discovery of a new particle, is thought to help researchers understand the powerful interaction (strong force), one of the four known fundamental interactions in physics. Other basic forces are gravitational force, electromagnetic force and weak interaction. The DZero scientists give a name X(5568) to this particle when they saw their first clue to this new particle in July 2015, because the mass was 5568 mega electron volts [1]. Quarks are basic particles that exist in two or three packages. The most famous of these are the proton and neutrality, each consisting of 3 quarks. But there are six types of quarks: up, down, weird, charm, bottom and top. They also each have antimatter.

On the other hand, A group of researchers from the Joint Quantum Institute in the USA and theoretical physicists from the National Institute of Standards and Technology (NIST) conducted an interesting study. According to a report in the Nanowerk, with this work, a step was taken to build objects out of the photons. Researchers who have found that photons, which are massless particles of light, can join a molecule with their own strength, showed that the two photons could be interlocked within a short distance. That is, under certain conditions, these photons can form a structure similar to two atomic molecules.

Finally, theoretical physicists have proved the process of attaching the article "Coulomb bound states of strongly interacting photons" in Physical Review Letters through several parameters [2]. According to this study, this bonding occurs when the photons can move side by side at a certain distance from each other. This process is similar when two hydrogen atoms in a hydrogen molecule are adjacent to each other. Alexey Gorshkov of theoretical physicists says, "It is not a molecule on its own, but it can be thought of as having a similar structure".

As far as the interaction engineering between photons is concerned, further advances can be gained for the technologies in these fields. For industry, bound and entangled photons can enable computers that use photons as their data processors. In fact, this can also provide significant energy savings. Because correspondence and other data exchanges move through fiber optic cables in the form of bundles of light, but they must be converted to electrons for processing. This process is an inefficient process in which a significant amount of electricity is used. Therefore, energy losses can be reduced if the photons are used again in place of transformation in the processing of the data.

Developments in the field of nanomaterials seem to change the luck of thermoelectric materials. Thermoelectric materials have become a promising technology for generating electricity from the heat that is thought to be lost. The basic logic of these thermoelectric materials is an electric current generated by the temperature difference between the two ends of

the material. Therefore, it may be possible to produce electrical currents from computers, automobiles, etc. made of these materials.

According to a paper published in Applied Materials and Interfaces, researchers have found that is allowing the material to generate electric current even at room temperature, when a small amount of graphene is applied to the thermoelectric material named strontium titanthritide (STO), because STO could generate electric current at extremely high temperatures [3]. The graphene causes this big difference. Energy efficiency is very low in traditional thermoelectric materials. It is around one percent. With the addition of graphite, researchers report this yield to be between 3 and 6 percent.

These studies have great importance because about 70 percent of the fuel used for a car loses to heat and friction. If such materials are available, a significant increase in energy efficiency can be achieved by recovery of the thermal energy.

References

[1] Dmitri Denisov and Paul Grannis, DZero discovers a new particle consistent with a tetraquark. (2016).

[2] M. F. Maghrebi, M. J. Gullans, P. Bienias, S. Choi, I. Martin, O. Firstenberg, M. D. Lukin, H. P. Büchler, A. V. Gorshkov, Coulomb bound states of strongly interacting photons, Physical Review Letters. (2015).

[3] Yue Lin, Colin Norman, Deepanshu Srivastava, Feridoon Azough, Li Wang, Mark Robbins, Kevin Simpson, Robert Freer, and Ian A. Kinloch*, Thermoelectric Power Generation from Lanthanum Strontium Titanium Oxide at Room Temperature through the Addition of Graphene, ACS Applied Materials and Interfaces. 7 (2015) 15898-15908.

Full Research Article | Submit Manuscript

Turkish Journal of Materials

Performance of mortars incorporating fly ash, silica fume, blast furnace slag at different temperature in magnesium sulfate solution

İlker Ustabaş[1,*], Şakir Erdoğdu[2]

[1]Department of Civil Engineering, Recep Tayyip Erdoğan University, 53100, Rize, Turkey
[2]Department of Civil Engineering, Karadeniz Technical University, 61000, Trabzon, Turkey

Received: 19/08/2016; Accepted: 01/12/2016; Published: 31/12/2016
Turk. J. Mater. Vol: 1 No: 1 Page: 1-14 (2016) ISSN: XXXX-YYYY
SLOI: http://www.sloi.org/sloi-name-of-this-article
*Correspondence E-mail: ilkerustabas@gmail.com

ABSTRACT This study presents the performance of five different mortars at room temperature, 40ºC and 5ºC in magnesium sulfate solution. Two groups of mortars are prepared of only cement but vary in ratio water/ cement (W/C) (0.52 and 0.625). The other three groups of mortars produced incorporating fly ash (FA), silica fume (SF) and blast furnace slag (BFS). These mortars were immersed for 600 days in magnesium sulfate solution. All mortars measured compressive strength, flexural strength during the 600 days. Water absorption and sorption of mortars were determined at 28 days. Microstructures of mortars were studied by scanning electron microscope (SEM) and microscope. Chemical analyzes were done with X-ray diffraction (XRF). Mortars sulfate attack affected mineral additives but cement prevent the mortars better than these with mineral additives. Mortars water absorption and sorption are important parameters on sulfate attack. Mortars corrupt at room temperature more than the other mediums.

Keywords: Magnesium sulfate; Brucite; Ettringite; Absorption; Sorption; Mineral additives; Silica fume; White materials.

Cite this article: İ. Ustabaş, Ş. Erdoğdu. Performance of mortars incorporating fly ash, silica fume, blast furnace slag at different temperature in magnesium sulfate solution. Turk. J. Mater. 1(1) 1-14 (2016).

1. INTRODUCTION

Sulfate attack is the term used to describe a series of chemical reaction between sulfate ions and the components of hardened concrete, principally the cement paste, caused by exposure of concrete to sulfates and moisture [1]. The sulfate attack can be divided into two groups of sulfate, 1-internal and 2-external sulfate attack. Internal sulfate attack refers to a situation where the source of sulfate is internal to concrete. The source of sulfate can be the cement, supplementary materials such as fly ash or slag, the aggregate, the chemical admixtures, or the water. Two examples of such internal sulfate attack by an excess of cement sulfate and the so-called delayed ettringite formation (DEF). External sulfate attack is caused by a source external to concrete. Such sources include sulfates from ground water, soil, solid industrial waste, and fertilizers, or from atmospheric sulfate (SO_3), or from liquid industrial wastes [1]. These two types of sulfate attack convert hardness concrete component into the other products, such as gypsum ($CaSO_4 2H_2O$), ettringite ($6CaO.Al_2O_3.SO_3.32H_2O$) and thaumasite ($CaSO_4.CaSiO_3.15H_2O$). These three kind of products are the main formation besides other products which occur to produce a kind of sulfate ion, such as brucite ($Mg(OH)_2$), magnesium silicate ($MgO.SiO_2.H_2O$) and hydrous silicate.

New product formation in hardness concrete consists of expansion, cracking and spilling. Sulfate attack decreases the durability of concrete, hereby long-term durability of structures is reduced and at the same time increases the cost of caring for structures, so the durability problems of concrete has drawn the attention of researchers.

The proposed mechanism of magnesium sulfate attack, sulfate ions firstly attack calcium hydrates and rapidly form brucite ($Mg(OH)_2$) and gypsum. Areas of concrete are touched by a solution of sulfate ions occur brucite layer and that behind gypsum layer [2].

$$Mg^{2+} + SO_4^{2-} + Ca(OH)_2 + 2H_2O \rightarrow Mg(OH)_2 + CaSO_4 2H_2O$$

When penetrated sulfate ions attack calcium silicate (C-S-H), the main corruptive product in hardness concrete begins to dangerously corrupt and C-S-H change magnesium silicate (M-S-H). hardness concrete transforms into a mud like substance.

$$xMg^{2+} + xSO_4^{2-} + x.CaO.SiO_2.aq + 3xH_2O \rightarrow x.CaSO_4.2H_2O + xMg(OH)_2 + SiO_2.aq$$

$$2xMg^{2+} + 2xSO_4^{2-} + 2[x.CaO.SiO_2.aq] + yH_2O \rightarrow 3MgO.2SiO_2.2H_2O + 2x[CaSO_4.2H_2O] + (2x-3).Mg(OH)_2$$

The sulfate attack corrupts concrete material and decreases the service life. Researchers are looking at how to protect concrete from sulfate ions with mineral additives such as fly ash, silica fume and granule blast furnace slag [3-9]. The laboratory studies show some different results. Separate sulfate ions, mineral additive, water cement rate, temperature, ions concentration produce an unlikely situation. Skalny, Amoudi, Thomas, Akoz have reported on the resistance imparted by mineral additives increasing the sulfate resistance of concrete [1,4,8,10,11]. The other researchers, Lee said that silica fume had decreased the resistance of concrete against sulfate, the larger amount SF content the greater was the strength loss exhibited [9]. Some researcher represented that mineral additive change CH to C-S-H for magnesium sulfate direct influence C-S-H formation, mineral additive decreases sulfate resistant of mortars [14]. Cavdar has reported an increase in the resistant of hardness concrete mineral additives must be restricted to approximately 25-30% by mass to erosion [12].

The quality of concrete, specifically a low permeability, is the best protection against sulfate attack. Adequate concrete thickness, high cement contents, low water/cement ratio and proper compaction and curing of fresh concrete are among the important factors that contribute to low permeability [1]. The most important role is permeability of hardness concrete and mortars in a sulfate environment [1,7,13,17]. Permeable concrete is vulnerable to attack by almost all classes of aggressive agents [15].

At medium temperature, have shown an occurrences of sulfate attack on concrete which is progressive. If medium temperature is high, thaumasite can occur greatly [16]. The formation of favored at low temperatures and a temperature of around 5ºC is most favorable. Nevertheless, a formation of this phase at temperatures up to about 25ºC is possible. The rate of thaumasite formation drops off markedly at somewhere between 15ºC and 20ºC [16].

The researchers have tried to develop various approaches to estimate long-term durability of concrete structures subject to sulfate attack. The researchers improve some equations such as $DC=[0,11\ S^{0,45}][0,143t^{0,33}][0,204.e^{0,145C_3A}]$. Where DC is the degree of sulfate-induce corrosion, S is sulfate concentration, t is immersion period (days), C_3A is the presentence of tricalcium aluminate. The others produced the equation connect to diffusion coefficient. $X_s=1.86.\ 10^6\ C_3A\ (\%).([Mg]+[SO_4])D_i.t$ Where Di is diffusion coefficient, X_s is the location of the visible degradation zone [1]. These kind equations were constantly improved by the researchers.

In this study, the varied medium temperature effect of different mineral additives, fly ash, silica fume, granule blast furnace slag on magnesium sulfate attack was investigated.

2. EXPERIMENTAL

2.1. Materials

2.1.1. Cement component

The material used in mortars specimens are provided from locally resourced Turkish sources supplies. The cement is ordinary Portland cement, CEM 42,5 R. Granule ballast furnace slag was obtain from Karabuk Iron-steel Factory. Silica fume and fly ash are from Eletktroferrocrom in Antalya and Thermal Power Plant. Five types of mortars were produced. Cement was incorporated in fly ash, silica fume and blast furnace slag with ratio 20 % weight of cement. Table 1. demonstrates the chemical properties of cement and materials. Table 2. shows cements and additive materials mechanical and physical properties.

Table 1. Chemical properties of cement and additive materials.

Contents	Cement	Fly ash	Silica fume	Granule blast furnace slag
CaO	54.7	1.3	0.5	25.3
SiO_2	24.9	57	95.3	43.3
Al_2O_3	5.3	1.1	0.7	13.6
Fe_2O_3	3	4.3	0.9	0.3
MgO	1.6	16.3	1.4	10.5
SO_3	3.3	0.4	0.4	3.7
Na_2O	0.9	0.4	0.3	0.2
K_2O	1.1	2.9	0.8	1.1
Cl^-	0.04	0.05	0.1	0

Table 2. Cements and additive materials mechanical and physical properties.

		Cement	Fly ash	Silica fume	Granule blast furnace slag
Density(g/cm^3)		3.05	2.4	2.2	2.7
Fineness(cm^2/g)		3832	3520	150000	4450
Loss on ignition (%)		3.5	1.67	3.34	1.38
Flexural strength (N/mm^2)	2 day	3.9			
	28 day	8.2			
Compressive strength (N/mm^2)	2 day	25.9			
	28 day	46.3			

2.1.2. Specimens preparation

The compositions of the mortars are shown Table3. All mixtures are used at the same aggregate, shown grading and physical properties in Table 4 and the ordinary Portland cement, CEM I 42,5 R. This cement is a mixture of three mineral additives, fly ash, silica fumes and granule blast furnace slag in some mortars. Mortar samples were prepared by Hobart mixer and mortar was placed on the impact test bench and were blocked in a mould to be 4*4*16 cm, 60 drops (twice). After 24 hours of curing at 20 ºC by 90% relative humidity, the samples were removed from the molds and placed in standard curing condition in statured lime water at 20±1ºC. Five main different types of mortars were prepare to mix with cement, fly ash, silica fume and granulated blast-furnace slag, using only cement mortars consisting of 480 g cement, and 250 g water (W/C=0,52), mortars, named PCM-1were used in 400 g cement and 250g water, W/C ratio is 0,625. Four mortars, FAM, SDM, BFSM and PCM-2 were kept at the same level water/binder ratio, 0,52. In additive mortars, with fly ash, silica fumes and blast furnace slag was incorporated with a ratio 20% weight of cement. In total five sets of mortars were prepared. Table 3 is shown at PCM-1, without mineral additive and 400 g cement, FAM, fly ash additive, SDM, silica fumes additive and BFSM, granule blast furnace slag additive mortars and PCM-2, mortars in 480 g cement.

Table 3. Mixture proportion of mortar specimens (1 m³).

Materials	Mortar specimens code of series				
	PCM-1	FAM	SFM	BFSM	PCM-2
Aggregate (kg/m^3)	1543	1455	1448	1465	1474
Cement(kg/m^3)	400	400	400	400	480
Water(kg/m^3)	250	250	250	250	250
Fly ash(kg/m^3)	0	80	0	0	0
Silica fume(kg/m^3)	0	0	80	0	0
Blast furnace slag(kg/m^3)	0	0	0	80	0

Table 4. Grading and physical properties of aggregate.

Aggregate type	Percentage passing						Density (g/cm^3)	Water absorption (%)
	Sieve size (mm)							
	8	4	2	1	0.5	0.25		
Fine aggregate	100	97	70	44	22	10	2.62	2.3

2.1.3. Specimens curing

After 24 hours, the specimens were removed from the molds and marked for later identification. All mortars were cured in lime saturated water 20±1ºC on one mount. Three specimens from all groups were measured for flexural and compressive strength for seven days. After one month, three mortars of groups were calculated for flexural and compressive strength, water absorption and sorption coefficient. The remaining specimens were divided into three groups and placed in a magnesium sulfate solution at room temperature, at 40ºC and at 5ºC for a period of 600 days.

Table 5. Specimens flexural and compressive strength.

Days	Mortar specimens									
	PCM-1		FAM		SDM		BFSM		PCM-2	
	7 days	28 days	7 days	28 days	7 days	28 days	7 days	28 days	7 days	28 days
Flexural strength (N/mm^2)	4.9	6.3	4.9	6.7	5.9	7.1	5.9	7.4	5.9	7.1
Compressive strength (N/mm^2)	30.5	37.9	33.2	42	38.9	46.6	31.3	53.1	33	53.2

Table 6. Compressive strength of mortars in sulfated medium (MgSO4), different temperature.

Medium	Date (mount)	Compressive strength (MPa)				
		PCM-1	FAM	SDM	BFSM	PCM-2
Room temperature	3	40.8	44.6	48.6	55.4	54.6
	6	36.4	44.2	47.8	55.6	54.1
	9	28.6	38.3	45.4	55.1	53.3
	12	18.8	32.4	42.3	53.2	51.8
	20	9.6	24.6	39.2	46.6	47.2
40ºC	3	41.2	45.4	48.9	55.2	54.9
	6	38.3	45.1	48.8	55.4	54.6
	9	35.9	43.4	47.5	54.8	53.8
	12	31.8	38.6	44.2	49.8	52
	20	22.1	28.4	39.2	47.5	48.8
5 ºC	3	40.2	44.3	48.4	55.1	54.2
	6	37.6	43.4	48.1	53.6	53.7
	9	31.5	39.6	44.4	46.7	49.6
	12	22.4	34.3	39.8	44.2	48.8
	20	15.4	26.5	34.8	40.1	47.8

Table 7. Flexural strength of mortars in sulfated medium (MgSO4), different temperature.

Medium	Date (mount)	Flexural strength (MPa)				
		PCM-1	FAM	SDM	BFSM	PCM-2
Room temperature	3	6.8	7.3	7.8	8.2	7.9
	6	6.1	7.2	7.8	8.1	7.9
	9	5.2	7	7.7	8.1	7.8
	12	3.4	6.5	7.4	7.8	7.7
	20	2.2	5.2	6.2	6.8	6.9
40ºC	3	6.9	7.4	7.9	8.1	7.8
	6	6.6	7.4	7.8	8	7.7
	9	5.8	7.3	7.6	7.9	7.6
	12	4.9	6.9	7.2	7.6	7.5
	20	3.8	5.8	6.6	6.9	6.9
5 ºC	3	6.8	7.2	7.7	8	7.8
	6	6.4	7	7.6	7.9	7.7
	9	5.1	6.9	7	7.3	7.1
	12	4.4	6.6	6.9	7.6	7
	20	3.6	5.6	6.5	7	6.9

2.1.4. Testing program

Specimens from all groups were tested on the 7th and 28th day flexural and compressive strength. After placed in three different environments of magnesium sulfate solution, three specimens from all series also were tested for flexural and compressive strength on 90th, 180th, 270th, 360th and 600th day. When mortars were taken from the curing pool, water of mortars were wiped and kept humid. Firstly, flexural strength was measured, after all pieces of mortars were tested by a mortars compressive test machine.

After one month, standard curing, specimens were measured for water absorption and sorption coefficient. For sorption, prisms of 40x40x160 mm were cast from each mixture, 28 days. Measurement of capillary sorption, three mortars specimens from each one group was stood in a oven at 70ºC until a constant mass formed. The bottoms of the mortars were opened and 3 mm above of mortars were covered by paraffin

The mortars were then placed in a pan. The water level in the pan was maintained at 3 mm above the base of the specimens throughout this experiment. All specimens were weighted at specific times such as 1, 2 4, 6,12 and 24 hours. The coefficient (k) was obtain by $(Q/A)= k.\sqrt{t}$ where Q= the amount of water adsorbed in (cm^3), A is the cross section of specimen that was in contact with water (cm^2), t is time (s), sorption coefficient is $cm/s^{1/2}$.

When mortars specimens were placed in three different solution pools, white materials (brucite and gypsum) began to change at different rates. Standing for 60 days, three mortars, PCM-1 in the different medium were cut into small nine pieces. New formations were observed under the microscope, taking 10 measurements from each one and calculated average thickness. Used Nikon SMZ 1000 type microscope and taking photography. NIS-elements program calculated white materials on mortars surface.

After placing in a magnesium solution, changes in all mortars were observed and photographed, some formations were investigated by microscope. Standing for 600 days in a sulfate solution, mortars specimens

were investigated by Scanning Electronic Microcopy (SEM) and X-Ray Diffraction (XRD). 5x5x3 mm small pieces were cut from the mortars. The pieces were dried in an oven and covered with gold than after investigated with SEM.

At room temperature, of 40ºC and at 5ºC, the pH of standing pools was measured together with temperature and conductibility. A group of mortars were put into the standard pool and this pool's pH, temperature and conductivity were also measured.

2.1.5. Solutions sulfate concentration

During the experimental program, magnesium sulfate solution concentration was adjusted to be added $MgSO_47H_2O$, 4.5 % of water weight. This medium is renewed with each mount.

3. RESULTS

Table 5. shows the compressive and flexural strength at the 7th and 28th of standard curing. Value of compressive and flexural strength at room temperature, 40ºC and 5ºC in magnesium sulfate solution are reported in Table 6 and Table 7. Fig.1, Fig.2 and Fig.3 are drawn according to Table.5, Table.6 and Table.7.

Fig.1. indicates the change of compressive strength at room temperature in magnesium sulfate solution. The change of compressive strength were calculated by the compressive strength at the 28^{th} days (R_{c28}) were eliminated from the compressive strength at the 90^{th},180^{th}, 270^{th}, 360^{th} and 600^{th} days (R_{Cx}) , and divided by the compressive strength at the 28^{th} days and multiply by 100 ($100x(R_{c28}-R_{cx})/ R_{c28}$) . The same calculations were made regarding the changes of the compressive and flexural strength in Fig.2, Fig.3, Fig.4, Fig.5 and Fig.6.

In Fig.1, during the first 90 days there are steady but slow increases in the all mortars, about %8 ratio, hereby R_{c28}. The next 180 days, compressive strength decreases slowly but next following days, compressive strength decreases quickly. Ratio of changing compressive strength of PCM-1 is 75% during 600 days. The mortars occurred high level corruption in PCM-1. There are high ratio of W/C (0,625), water absorption (10,5%) and sorption coefficient ($21,8x10^{-3}$) in PCM-1. PCM-1 also has the less weight of cement and compressive strength (R_{c28}=37,9 N/mm^2). Fig.1. indicated that mortars, to be high W/C, water absorption and sorption, affected much more than the others in magnesium sulfate solution. The corruption of FAM is second, ratio of 48% according to fig.1. FAM has second high water absorption and sorption but FAM has same ratio of W/C, with BFSM, SDM and PCM-2. FAM, used fly ash mineral additive, fineness of fly ash is smaller than blast furnace slag and silica fume (Table.2). If fineness is low at the mineral additives, the mortars have much water absorption and sorption on the 28 days. This situation is demonstrated Fig.7 and Fig.8. Third corruption has in BFSM, ratio of 12%. Fourth corruption has in SDM, ratio 10%. Value of changing compressive strength in SDM is very near the value in BSFM. The best performance is shown in PCM-2. There is no any mineral additive in PCM-2, but has maximum cement content, 480 kg/m^3 and low water absorption (9,3%) and sorption ($17,2x10^{-3}cm/s^{1/2}$) (Table 8). When PCM-2 is compared PCM-1, low ratio of W/C, water absorption and sorption increase the resistant of mortars on sulfate attack. Fig.1, Fig.7 and Fig 8 exhibit that the higher cement content causes less water absorption and sorption at the same ratio of W/C and aggregate. The arrangement of changing compressive strength in fig.1. has a similar arrangement water absorption and sorption, Fig.7 and Fig.8. This evidence shows that water absorption and sorption in mortars is the best parameter against magnesium sulfate attack.

In Fig.2 and Fig.3 are shown a shape like Fig.1 but the ratios of changing compressive strength are different. While the ratio of changing compressive strength in PCM-1at room temperature is 75%, it is 42% at 40ºC and 60% at 5ºC. The same situation is shown in the ratio of changing compressive strength at FAM, BFSM, SDM and PCM-2. The high corruption occurred at room temperature in magnesium solution after than at 5 ºC. The best performance of mortars is at a high temperature at 40ºC. This evidence was derived from occurrences between new materials formation and pH at different temperature medium. Fig.9. shows four types curing conditions of mortars, at room temperature, 40ºC, 5ºC in magnesium sulfate solution and standard curing pool, no sulfate, were detected on the first day, nearly equals values were at the same levels, more with values of pH at 40º (Table 9). Values of pH at 5ºC in magnesium solution had increased during 30 days. Values of pH at 5º were higher than the others mediums. If pH is high, concrete and mortars decomposes less. Fig.10. white material on surface of mortars can be seen where a white color is easily identified under the microscope. Fig.11.. depicts how this thickness was measured by Nıs–elements D, computer program. Results of the measurement, thickness of white materials at 40º in magnesium sulfate solution was higher and quicker than in the other mediums. This situation indicates warm water increased the reaction between cement materials and sulfate. The thickness of white materials was the thinnest at a low temperature of water. Thickness of white materials is given in Table 10 for each medium at 90 days. Fig.12. gives results of XRD. This analyze was done on white materials, taken from surface on mortars in magnesium sulfated solution. In this analyze many peaks relating to brucite and gypsum were found.

The ratio of compressive strength, pH of solution and speed of white materials formation were analyzed with an expectations high corruption at 40º in magnesium solution for low value of pH, but thickness and quick white

materials formation reduce permeability and starts corruption later. High pH prevented the mortars at 5ºC, so the mortars deteriorated at room temperature in magnesium sulfate solution, firstly.

Fig.13, , Fig.14 and Fig.15 show SEM micrograph of PCM-1, at 600 days, at room temperature, 40ºC and 5ºC in magnesium sulfate solution. Fig.16. indicates the result of XRD. Which mortars had the greatest damages from sulfate, new materials formation increased in Fig.13, Fig.14, and Fig.15. How sulfated solution entered into void and crack, SEM micrograph were showed. New material formation cause expansion and cracking in mortars, are shown at SEM analyze. Ettringite, thaumasite and gypsum were found by XRD.

Table 8. Mortar specimens sorptivity coefficient and water absorption at 28 days.

Specimens type	Water absorption (%)	Sorptivity coefficient (cm/s$^{1/2}$)
PCM-1	10.5	0.02361
FAM	10.3	0.021844
SDM	9.8	0.019322
BFSM	9.9	0.018959
PCM-2	9.3	0.017284

Table 9. Curing pool pH, temperature and mV values.

Time (day)	Room temperature with $MgSO_4$			40ºC with $MgSO_4$			5ºC $MgSO_4$			Standard curing		
	pH	ºC	mV	pH	ºC	mV	pH	ºC	mV	pH	ºC	mV
1	7.32	20.4	0.01	7.22	39.3	0.8	7.36	17.7	-0.01	7.81	19.8	-110
9	9.16	22.7	101	8.27	40.1	-0.59	8.75	4.9	-0.88	9.02	20.4	-107
24	8.77	20.9	0.94	7.92	39.6	-0.36	10.25	4.5	-185	8.94	20.3	-103
30	8.73	18.1	-100	7.85	39.5	-0.47	10.33	2.4	-187	8.76	19.4	-100

Table 10. White materials thickness is on PCM-1 mortars at 90 days in magnesium sulfate solution.

Group name	White materials thickness (micron)		
	Room temperature	40 ºC	5ºC
PCM-1	78.54	136.87	44.72

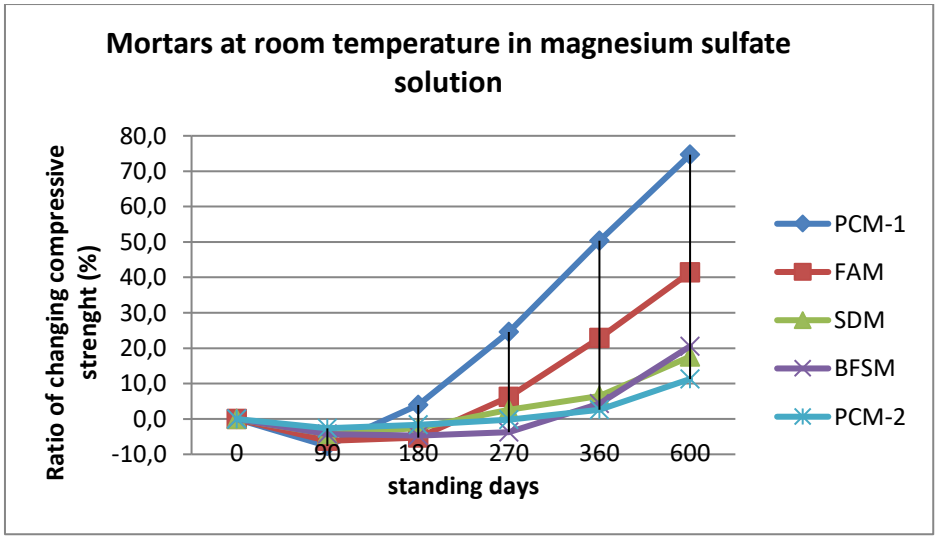

Fig.1. Mortars ratio of changing compressive strength at room temperature in magnesium solution

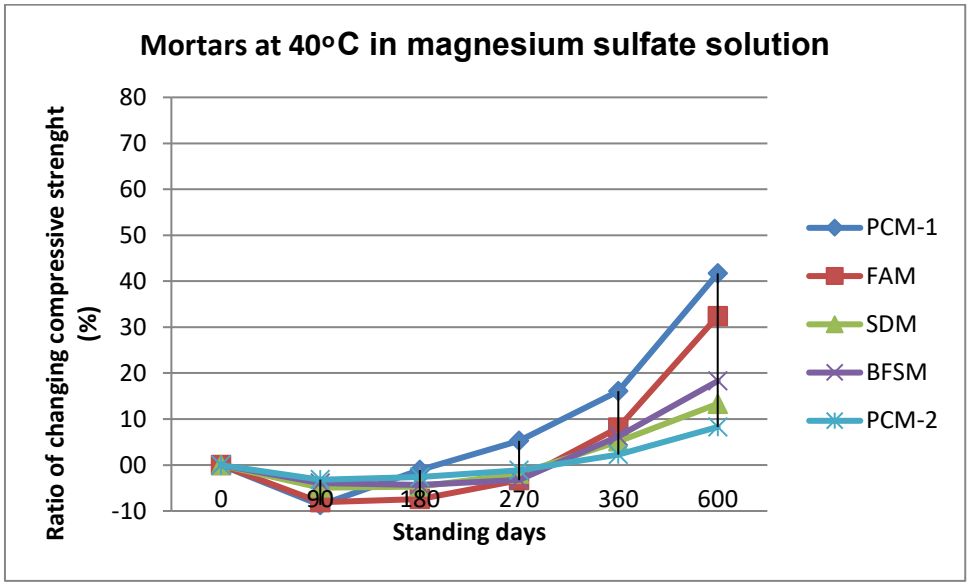

Fig.2. Mortars ratio of changing compressive strength at 40°C in magnesium solution

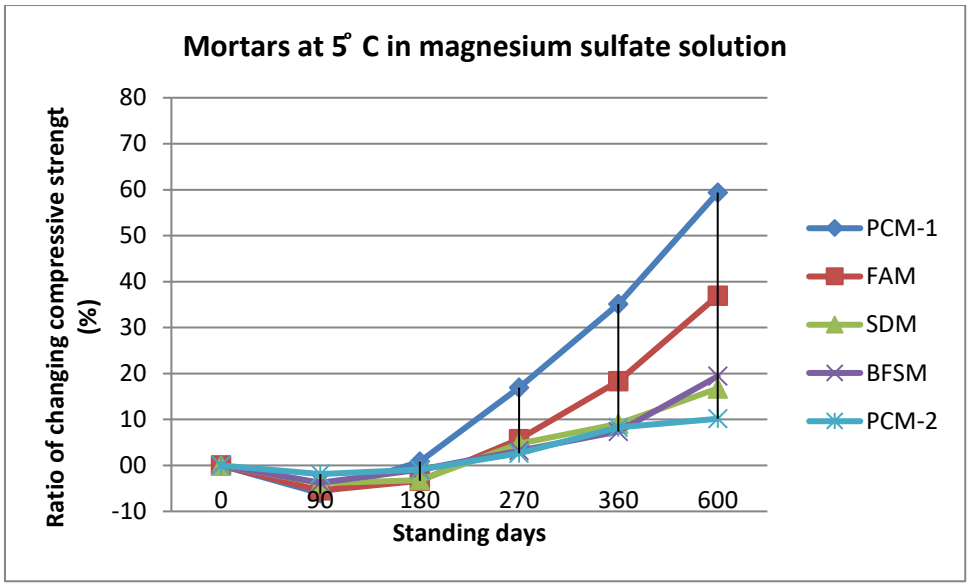

Fig.3. Mortars ratio of changing compressive strength at 5°C in magnesium solution

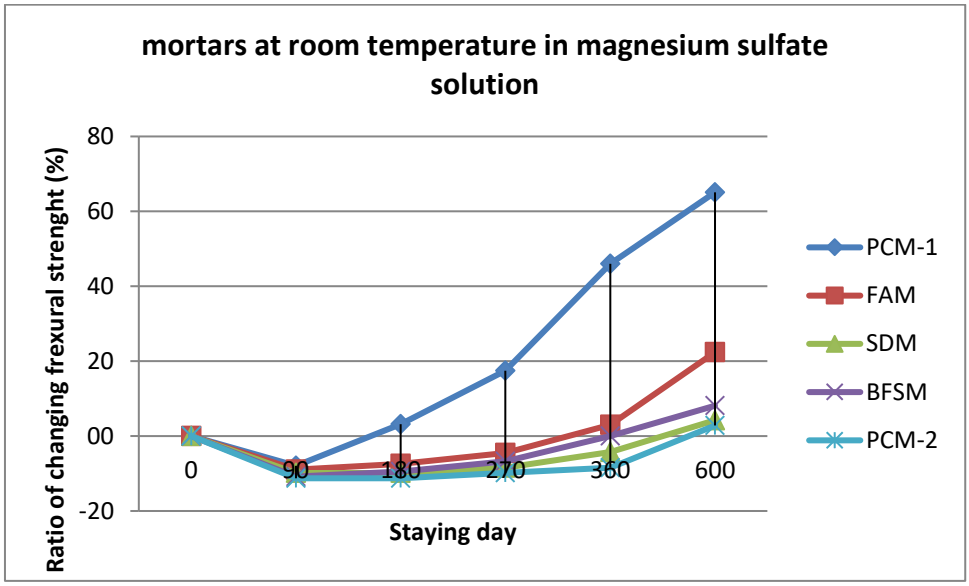

Fig.4. Mortars ratio of changing flexural strength at room temperature in magnesium solution

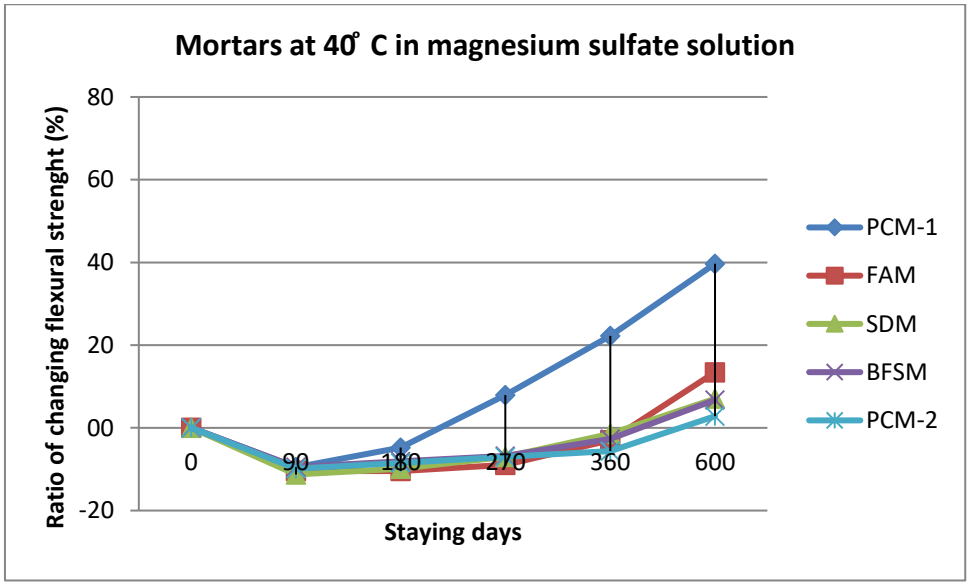

Fig.5. Mortars ratio of changing flexural strength at 40°C in magnesium solution

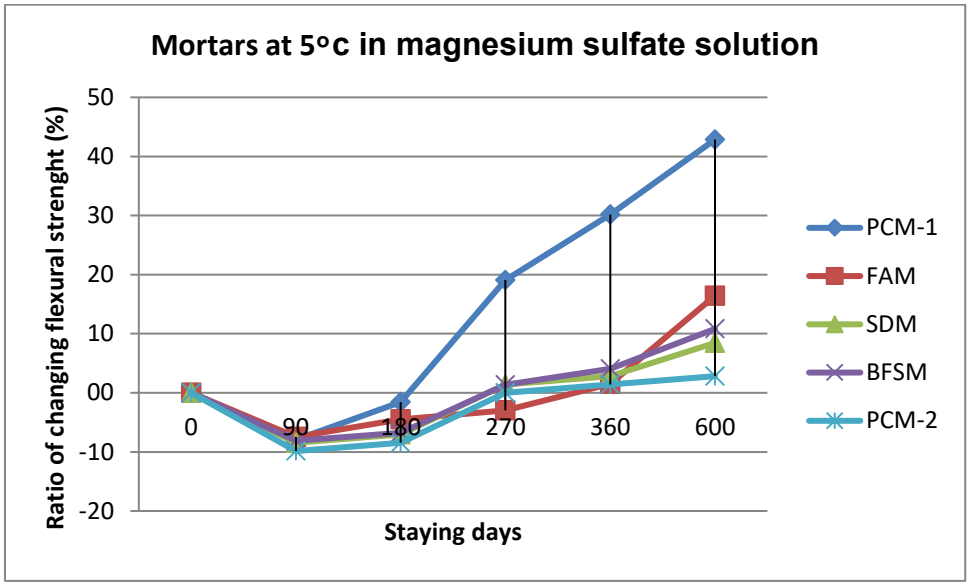

Fig.6. Mortars ratio of changing flexural strength at 5°C in magnesium solution

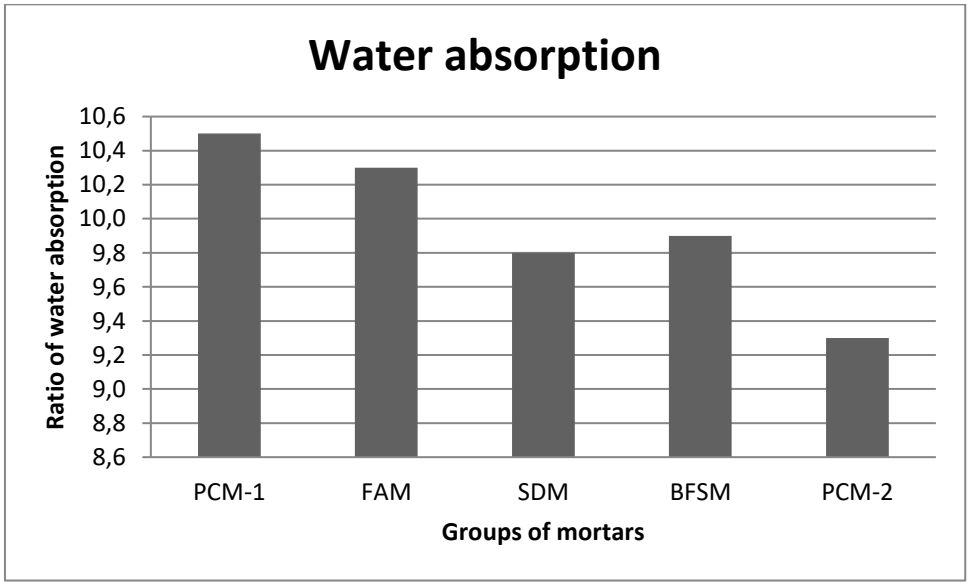

Fig.7. Group of mortars water absorption levels

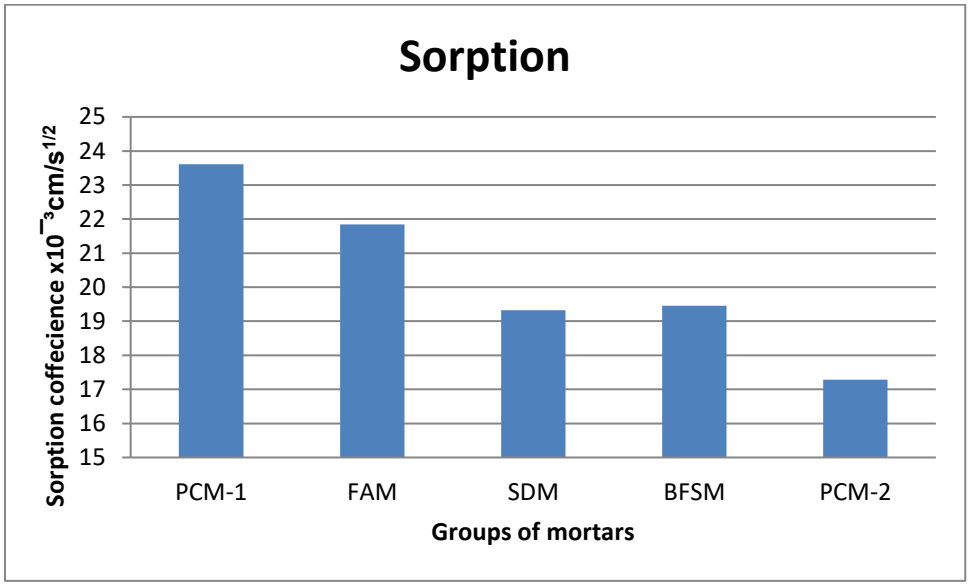

Fig.8. Group of mortars sorption coefficient levels

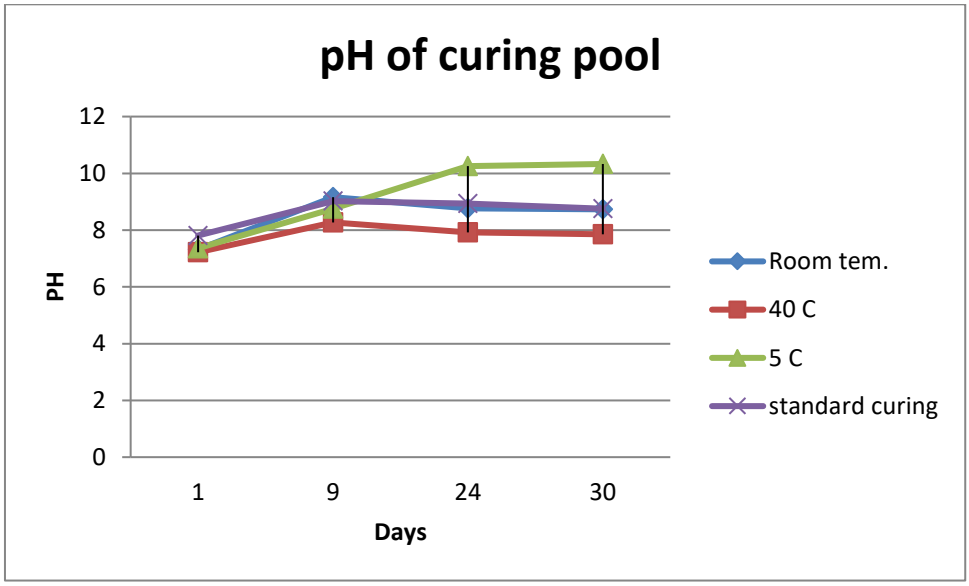

Fig.9. pH value of curing pool

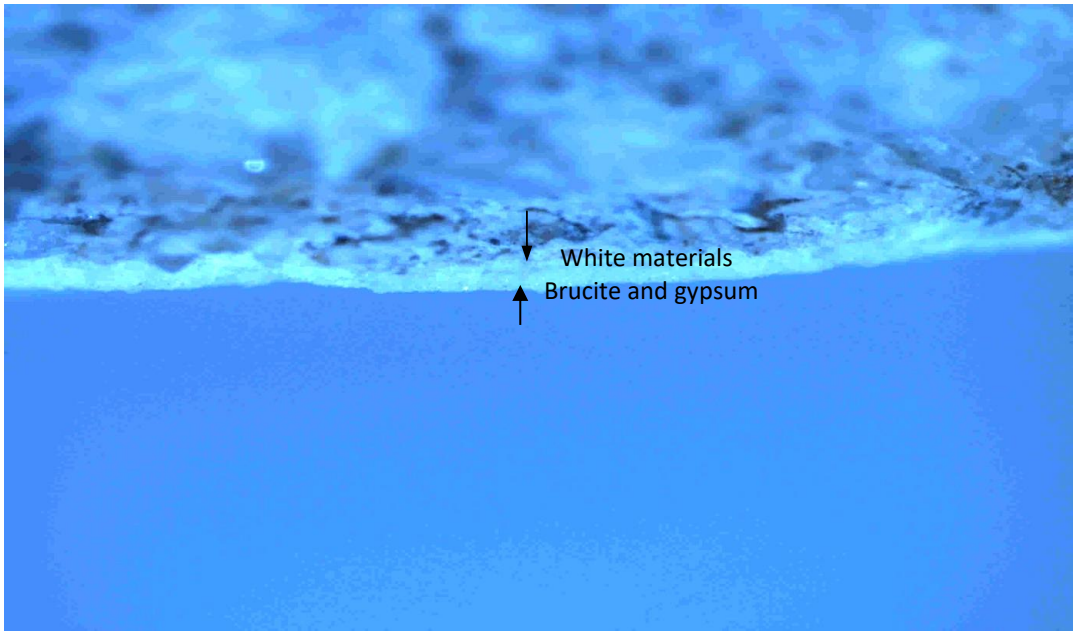

Fig.10. Occurrences of white materials on mortars

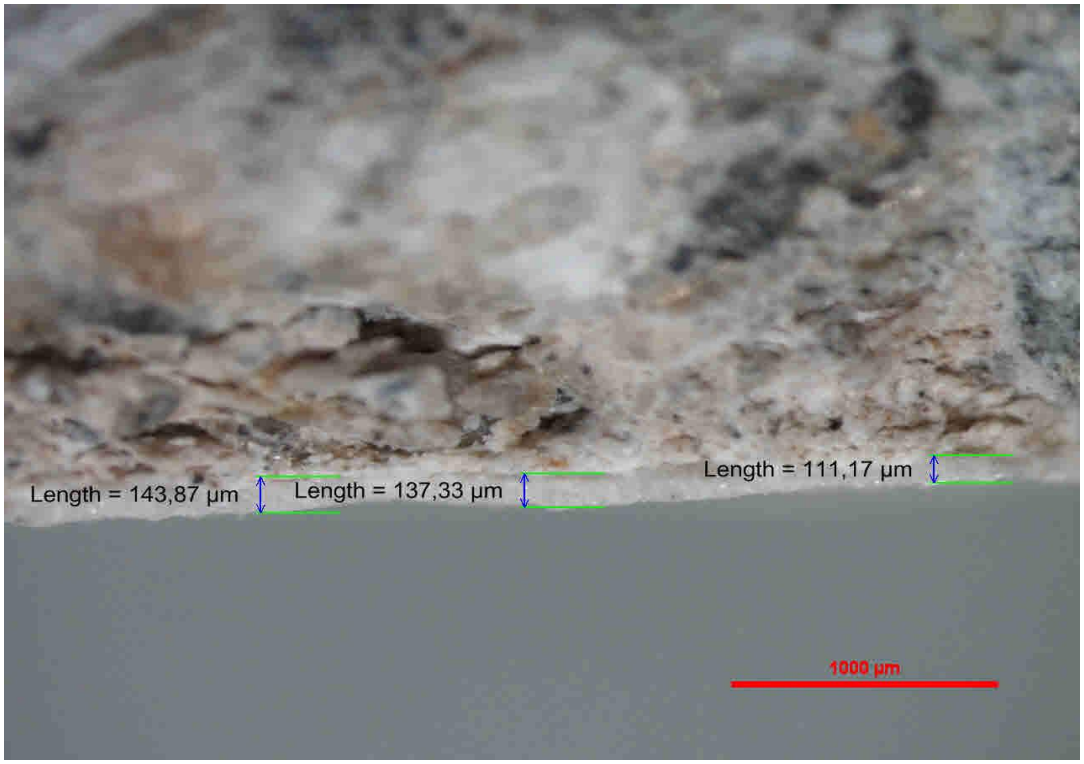

Fig.11. Thickness of White materials, standing 60 days at 40°C in magnesium sulfate solution on mortars.

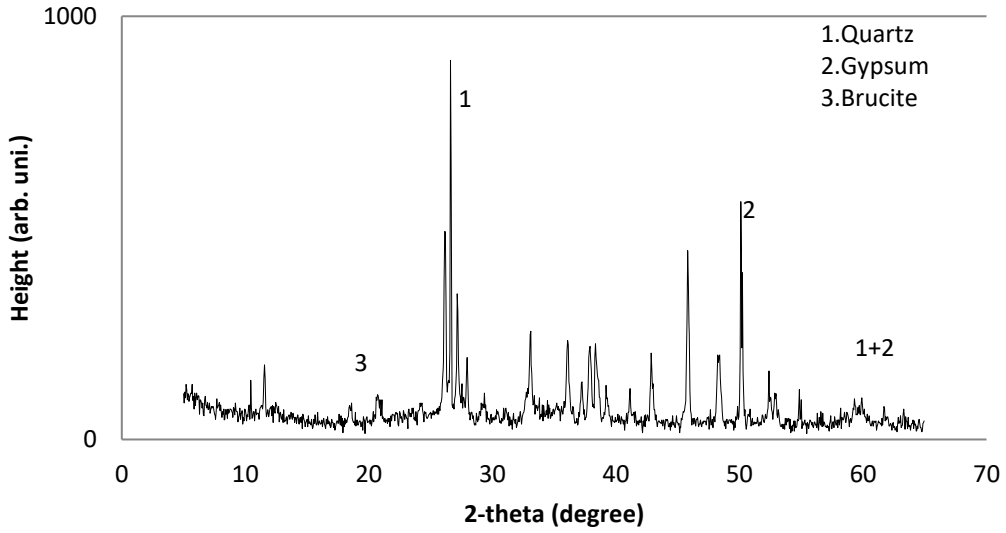

Fig.12. XRD of white materials

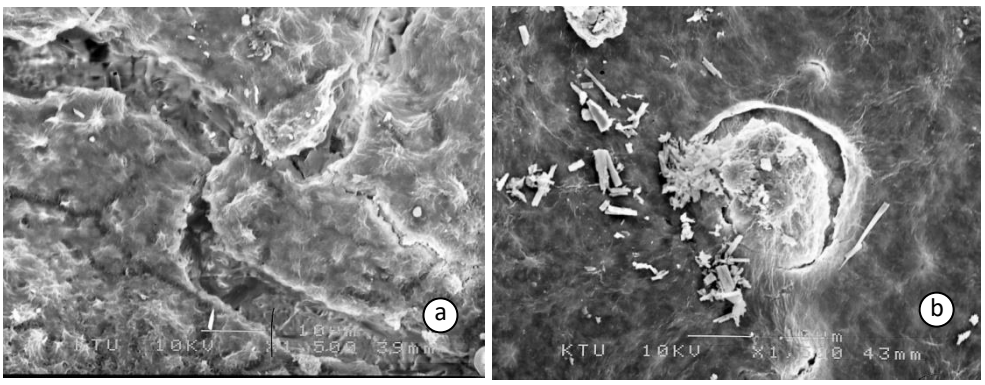

Fig.13. SEM micrograph of PCM-1, at 600 days, at room temperature in magnesium sulfate solution. (a) SEMx1500, (b) SEMx1500

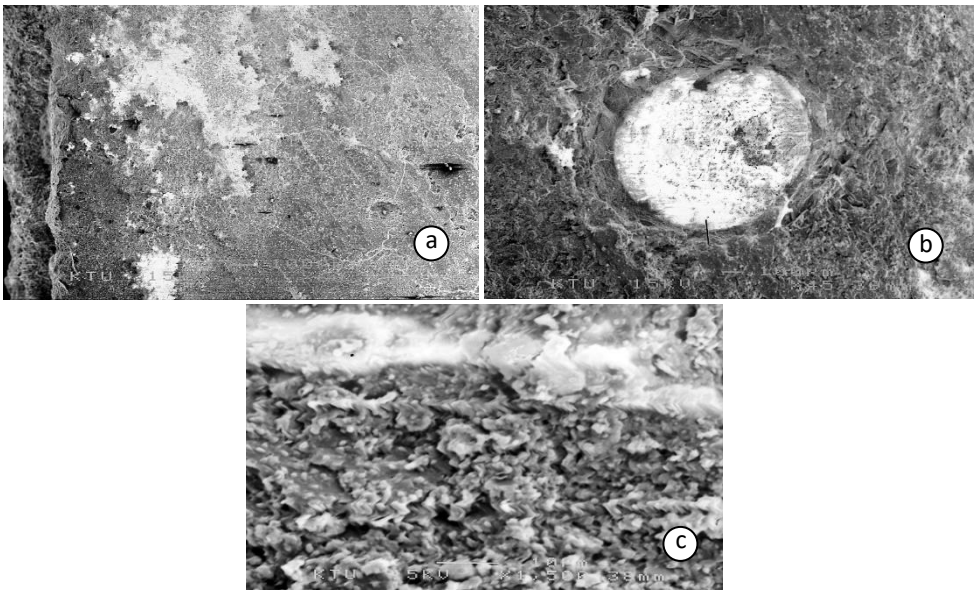

Fig.14. SEM micrograph of PCM-1, at 600 days, at 40^{o} in magnesium sulfate solution. (a) SEMx60, (b) SEMx45, (c) SEMx1500

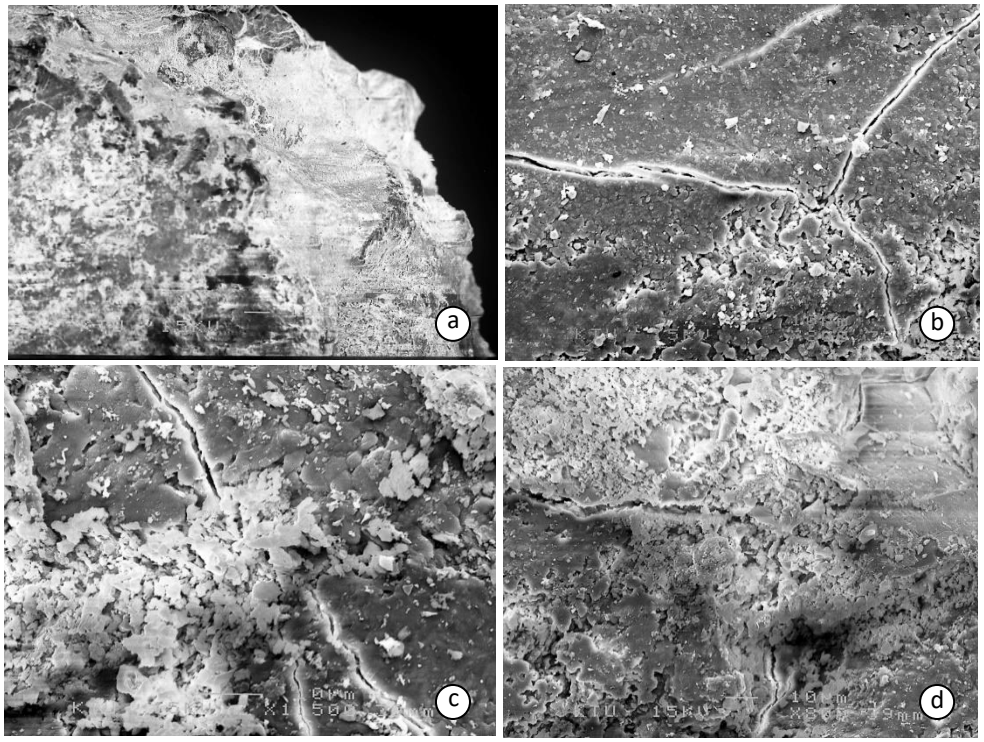

Fig.15. SEM micrograph of PCM-1, at 600 days, at 5º in magnesium sulfate solution. (a) SEMx60, (b) SEMx800, (c) SEMx1500, (d) SEMx800

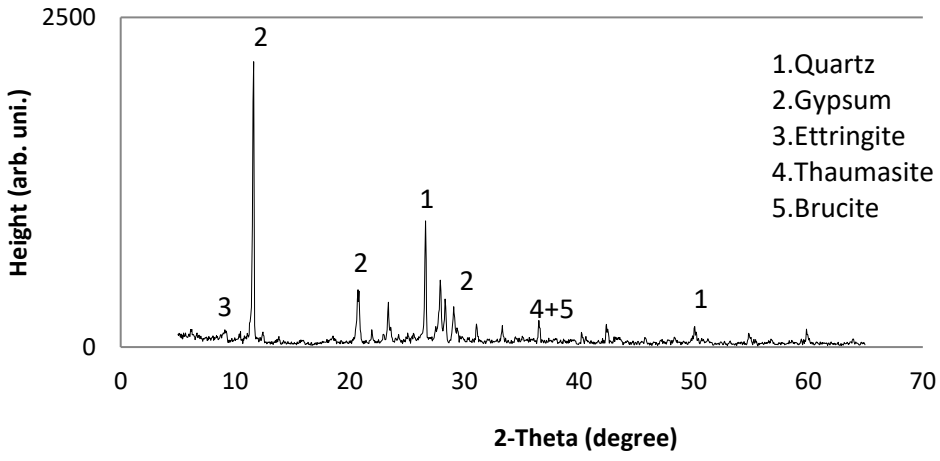

Fig.16. XRD of PCM-1 at room temperature.

4. CONCLUSION

The following conclusions can be made based on the test results of this study. Using the same types of aggregated and water/cement ratio, water absorption and sorption are important in magnesium sulfate attack. Mineral additive affected the absorption of mortars and prevent the mortars from magnesium sulfate attack. At the same ratio of W/C, high cement content mortars show the best performance in magnesium sulfate solution. With a less water /cement ratio reduce absorption therefore resistance of mortars increases against magnesium sulfate attack. Different temperature levels influence sulfate attack. The speed of occurring brucite and gypsum on mortars and pH levels of sulfate solution are the other parameters influencing magnesium sulfate attack. Mortars are affected at room temperature more than at 40ºC and 5ºC. Corruptions reduce at the same proportion of magnesium sulfate solution at high temperature. High temperature affected thickness and speed of formations, on white materials.

References

[1] J. Skalny, J. Marchand, I. Odler, Sulfate Attack on Concrete, Spon Press, New York (2002).

[2] M. Santhanam, M.D. Cohen, J. Olek. Mechanism of sulfate attack: a fresh look part 2. Proposed mechanisms. Cement and Concrete Research 33 (2003) 341-346.

[3] M. Abd El Aziz, S. Abd El Aleem, M. Heikal, H. Didamony, Hydration and Durability of Sulphate-Resisting and Slag Cement Blends in Caron's Lake Water, Cement and Concrete Research 35 (2005) 1592-1600.

[4] O.S.B. Al-Amoudi, Attack on Plain and Blended Cement Exposed to Aggressive Sulfate Environments, Cement & Concrete Composites 24 (2002) 305-316.

[5] E.F. Irassar, M. Gonzalez, V. Rahhal, Sulfate Resistance of Type V Cement with Limestone Filler and Natural Puzzolana, Cement & Concrete Composites 22 (2000) 361-368.

[6] M. Nehdi, M. Hayek, Behavior of Blended Cement Mortars Exposed to Sulfate Solutions Cycling in Relative Humidity, Cement and Concrete Research (2005) 735-742.

[7] M. Santhanam, M.D. Cohen, J. Olek, Effect of Gypsum Formation on the Performance of Cement Mortars During External Sulfate Attack, Cement and Concrete Research 32 (2003) 325-332.

[8] F. Türker, F. Akos, S. Koral, N. Yüzer, Effect of magnesium sulfate Concentration on Sulfate resistance of Mortars With and Without Silica Fume, Cement and Concrete Research, 27(2) (1997) 205-214.

[9] S.T. Lee, H.Y. Moon, R.N. Swamy, Sulfate attack role of silica fume in resisting strength loss, Cement & Concrete Composites 27 (2005) 65-75

[10] F. Akoz, F. Turker, S. Koral N. Yuzer, Effect of sodium sulfate concentration on the sulfate resistance of mortars with and without silica fume, Cement and Concrete Research 25 (1995) 1360-1368.

[11] M.D.A. Thomas, M.H. Shehata, S.G. Shashiprakash, D.S. Hopkins, K. Cail, Use of Ternary Cementations Systems Containing Silica Fume and Fly Ash in Concrete, Cement and Concrete Research 29 (1999) 1207-1214.

[12] A. Cavdar, Ş. Yelgin, Investigation of mechanical and mineralogical properties of mortars subjected to sulfate, Construction and Building Materials, 24 (2010) 2231-2242.

[13] P. Brown, R.D. Hooton, Ettringite and Thaumasite Formation in Laboratory Concretes Prepared Using Sulfate-resisting Cements, Cement & Concrete Composites 24 (2002) 361-370.

[14] A. Rasheeduzzafar, S.N. Abduljauwad, M. Maslehuddin, Mechanism of Magnesium-Sodium Sulfate Attack in Plain and Blended Cements, ASCE Mater Civil Engineering (1994) 201-222.

[15] A.H. Memon, S.S. Radin, M.F.M. Zain, J. Trottier, Effect of mineral and chemical admixtures on high-strength concrete in seawater, Cement and Concrete Research 32 (2002) 373-377.

[16] N.J. Crammond, The Thaumasite Form of Sulfate Attack in the UK, Cement & Concrete Composites 25 (2003) 809-818.

[17] G. Li, X. Zhao, Properties of concrete incorporating fly ash and ground granulated blast- furnace slag, Cement & Concrete Composites 25 (2003) 293-299.

Letter Article | Submit Manuscript

Turkish Journal of Materials

Electronic energy state and transmission properties study of parabolic double quantum well using Non-Equilibrium Green function method

M. Batı[1,*]

[1]Department of Physics, Recep Tayyip Erdoğan University, Rize, Turkey

Accepted: 23/11/2016; Published: 31/12/2016

Turk. J. M. Vol: 1 No: 1 Page: 15-18 (2016)

SLOI: http://www.sloi.org/sloi-name-of-this-article

*Correspondence E-mail: mehmet.bati@erdogan.edu.tr

ABSTRACT We apply the non-equilibrium Green's function method based on the finite difference method to the parabolic double quantum well structure. In particular, we examine the effect of system parameters on transmission coefficient. The properties of the electronic state also studied as a function of the system parameters, such as, the well widths and depth. We also tested energy electronic state with calculating density of states.

Keywords: Non-equilibrium Green Functions; Finite Difference Method; Parabolic Double Well; Transmission.

Cite this article: M. Batı. Electronic energy state and transmission properties study of parabolic double quantum well using Non-Equilibrium Green function method. Turk. J. Mater. 1(1) 15-18 (2016).

1. INTRODUCTION

According to Moore's famous law [1], states that the number of transistors on integrated circuits doubles every year. Last decades semiconductor devices already reached the limit to the nano-scale. The non-equilibrium Green's function (NEGF) method [2] are extensively used method for finding transmission properties in nanoscale devices.

Quantum wells are semiconductor structures in which we can observe and control many quantum mechanical effects. Recent developments in nanofabrication technologies have allowed us to fabricate variety type of wells. Such as, parabolic quantum wells (PQWs) which are related the development of high performance semiconductor devices (infrared detectors, cascade lasers, etc.) [3-6].
The properties of the electronic state in the PQW were studied in experimentally and theoretically [7,9]. Because of the unique properties (equally spaced electronic spectrum, radiative transitions at the same oscillator frequency etc.), researchers [10, 11] studied the electronic state in the PQW by using different methods to derive the energy levels. PQW has been widely investigated and some new properties of electrons are obtained [12, 13]. PQWs have been applied to study non-linear optical properties [14], the quantum Hall effect [15], charge, spin oscillations [16], magnetic properties and photoluminescence measurements [17, 18]. Capasso and Kiehl proposed a resonant-tunneling bipolar transistor with a smooth parabolic well [19, 20].

The aim of the present work is to study transmission properties and electronic states in one dimensional double GaAs/AlGaAs PQW using NEGF method.

2. MODEL AND METHOD

We apply the NEGF method to find electronic eigen-state and transmission characteristic of parabolic double quantum well (PDQW). As depicted in Fig. 1, L_i denotes the region boundary of the structure.

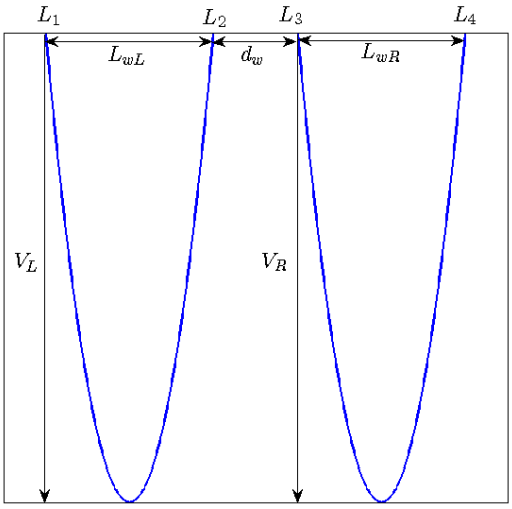

Fig. 1. Schematic representation of one-dimensional parabolic double quantum well.

An ideal parabolic potential well represents a "Harmonic oscillator well" which is described in quantum mechanics textbooks. One-dimensional PDQW potential can be written as

$$\boldsymbol{U(x)} = \begin{cases} \boldsymbol{a_L(x-(L_1+L_2))^2 - V_L}, & \boldsymbol{L_1 \le x \le L_2} \\ \boldsymbol{a_R(x-(L_3+L_4))^2 - V_R}, & \boldsymbol{L_3 \le x \le L_4} \\ \boldsymbol{0}, & \boldsymbol{odher\ wise} \end{cases} \quad (1)$$

where, $\boldsymbol{a_L} = \frac{\boldsymbol{V_L}}{\boldsymbol{(L_{wL})^2}}$, $\boldsymbol{a_R} = \frac{\boldsymbol{V_R}}{\boldsymbol{(L_{wR})^2}}$, left well width is $\boldsymbol{L_{wL}} = \boldsymbol{|L_2 - L_1|}$, and right well width is $\boldsymbol{L_{wR}} = \boldsymbol{|L_4 - L_3|}$ and distance between two well is $\boldsymbol{d_w} = \boldsymbol{|L_3 - L_2|}$. We use dimensionless form of the Schrödinger equation by using the Effective Bohr radius ($\mathbf{a_0^*}$) and Hartree energy ($\mathbf{E_H^*}$) for scales. So, Schrödinger equation becomes

$$-\frac{1}{2}\frac{d^2\psi}{d\tilde{x}^2} + \tilde{U}(\tilde{x})\psi = \tilde{E}\psi \quad (2)$$

Finite difference discretization method applied to the equation (2) as follows [2]:

$$-\tilde{t}\psi_{n-1} + \left(2\tilde{t} + \tilde{U}_n\right) - \tilde{t}\psi_{n+1} = E\psi_n \quad (3)$$

where $\tilde{t} = \frac{1}{2\Delta\tilde{x}^2}$ is the hopping parameters, and we use abbreviation $\tilde{U}_n = \tilde{U}(\tilde{x}_n)$. Including self-energies and considering matrix representations, the new form of Eq.2 becomes

$$[EI - H - \Sigma_L - \Sigma_R]\{\psi\} = \{S\} \quad (4)$$

where [H] is the Hamiltonian matrix [I] is the identity matrix, $\{\psi\}$ is the wave function vector and $\{S\}$ is scattering term vector. Σ_L and $\Sigma_R$are corresponding to the self-energies of the left and right contacts, respectively. Accordingly, [H] takes form as:

$$\begin{pmatrix} 2\tilde{t}+\tilde{U}_1 & -\tilde{t} & 0 & \cdots & 0 & 0 \\ -\tilde{t} & 2\tilde{t}+\tilde{U}_2 & -\tilde{t} & \cdots & 0 & 0 \\ 0 & -\tilde{t} & 2\tilde{t}+\tilde{U}_3 & \ddots & \vdots & \vdots \\ 0 & 0 & \ddots & \ddots & -\tilde{t} & 0 \\ \vdots & \vdots & \ddots & -\tilde{t} & 2\tilde{t}+\tilde{U}_{N-1} & -\tilde{t} \\ 0 & \cdots & 0 & 0 & -\tilde{t} & 2\tilde{t}+\tilde{U}_N \end{pmatrix}$$

In addition, self-energy terms $[\Sigma_L]$, $[\Sigma_R]$ and source term $\{S\}$ are given by

$$[\Sigma_L] = \begin{pmatrix} -\tilde{t}e^{i\tilde{k}_L\Delta\tilde{x}} & 0 & \cdots & 0 \\ 0 & 0 & & 0 \\ \vdots & & \ddots & \vdots \\ 0 & & \cdots & 0 \end{pmatrix},$$

$$[\Sigma_R] = \begin{pmatrix} 0 & \cdots & & 0 \\ \vdots & \ddots & & \vdots \\ 0 & & 0 & 0 \\ 0 & \cdots & 0 & -\tilde{t}e^{i\tilde{k}_R\Delta\tilde{x}} \end{pmatrix},$$

$$\{S\} = \begin{pmatrix} -\tilde{t}(e^{i\tilde{k}_L\Delta\tilde{x}} - e^{-i\tilde{k}_L\Delta\tilde{x}} \\ 0 \\ \vdots \\ 0 \end{pmatrix}.$$

There are several methods for finding the energy eigenvalues corresponding to a particular potential. One can use eigenvalues of [H] matrix to find energy eigenvalues. The retarded Green's function of the system is

$$[G^r] = [(E + i\lambda)I - H - \Sigma_L - \Sigma_R]^{-1} \quad (5)$$

where λ is an infinitesimally small positive number. Transmission coefficient T can be computed as

$$T = Tr[\Gamma_L G^r \Gamma_R G^{r+}] \quad (6)$$

Here, $\Gamma_L = i[\Sigma_L - \Sigma_L^+]$ and $\Gamma_R = i[\Sigma_R - \Sigma_R^+]$ are broadening functions. Finally, density of states (DOS) can be computed as follows

$$DOS = -\frac{1}{\pi} Im(Tr[G^r]). \quad (7)$$

3. RESULTS

Here, transmission coefficient (T) in parabolic quantum well structure is investigated, we assume the effective mass of the electron $0.067m_0$ to be constant through the system. The transmission coefficients are numerically evaluated across PDQW structure with different structure parameter. Lowest ten energy states for different structure parameters are presented in Tables. There are bound states and scattering state. Number of energy states is altering with changing structure parameters.

We examine the dependence of the transmission coefficient on the well width as depicted in Fig.2. We can see in Fig. 2 and also Table 1 number of energy levels (bound and scattering states) increases with increasing well width. We see that in Table2 because of the increment of well depth, the confinement becomes stronger and so number of bound state increases.

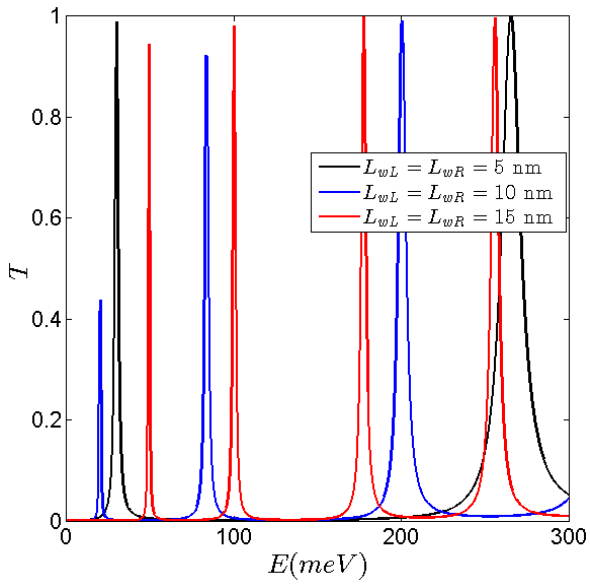

Fig. 2. Transmission probability versus electron energy. Structure parameter is V_L=V_R=150 meV 〖,d〗_w=1 nm

In order to illustrate the effect of well separation, we plot Fig.3 for $V_L = V_R = 150$ meV, $L_{wL} = L_{wR} =$ 10 nm. We can see that in Fig.3 and Table 3 energy level decreases with increasing well separation.

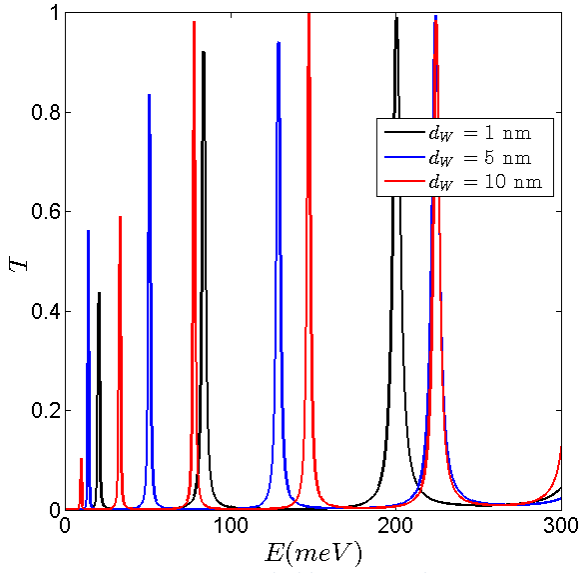

Fig. 3. Transmission probablity versus electron energy. Structure parameter is V_L=V_R=150 meV, L_wL=L_wR=10 nm

Density of states (DOS) is calculated for 5 nm, 10 nm and 15 nm symmetrical well width structures by calculating the diagonal elements of retarded Green's function. As shown in Fig.4 the first peak in the DOS for all structure is sharp and high. Energy level position is consistent to the T(E) in Fig.2. Existence of sharp resonance states are reported form the knowledge of density of states [16]. DOS also helps to predict the device performance.

Table 1. Eigen states of PDQW with different well width for V_L=V_R=150 meV, d_w=1 nm

$L_{wL} = L_{wR} = 5\ nm$ Eigen-states (E-S) (meV)	$L_{wL} = L_{wR} = 10\ nm$ E-S (meV):	$L_{wL} = L_{wR} = 15\ nm$ E-S (meV):	$L_{wL} = L_{wR} = 20\ nm$ E-S (meV):
-46.5	-93.7	-111.2	-120.7
-44.1	-80.3	-108.6	-120.1
295.3	242	-36.1	-63.1
579.6	213.3	-15.5	-56.9
965.4	341.2	52.6	-5.6
1427.3	502.6	105.8	17.9
1974.9	682.7	185.2	68.7
2607.1	890.1	266.7	112.3
3321.5	918.0	365.2	171.1
4122.4	1120.0	471.4	230.8

Table 2. Eigen states of PDQW with different well depth for L_wL=L_wR=10 nm, 〖d〗_w=1 nm

$V_L = V_R = 150\ meV$ Eigen-states (E-S) (meV)	$V_L = V_R = 300\ meV$ E-S (meV):	$V_L = V_R = 600\ meV$ E-S (meV):	$V_L = V_R = 900\ meV$ E-S (meV):
-93.7	-217.7	-482.7	-756.3
-80.3	-211.9	-481.2	-755.8
24.2	-58.8	-250.6	-469.4
91.8	-13.6	-233.2	-462.4
213.3	129.8	-25.7	-190.0
341.2	245.7	52.4	-146.1
502.6	413.7	246.5	92.7
682.7	590.0	405.7	221.3
890.1	799.3	622.9	454.9
1120.0	1028.0	845.8	665.5

Table 3. Eigen states of PDQW with different well separation for 〖V_L=V〗_R=150 meV, L_wL=L_wR=10 nm

$d_w = 1\ nm$ Eigen-states (E-S)(meV)	$d_w = 5\ nm$ E-S(meV):	$d_w = 10\ nm$ E-S(meV):	$d_w = 20\ nm$ E-S(meV):
-93.7	-88.6	-87.4	-87.2
-80.3	-85.8	-86.9	-87.2
24.2	16.5	10.9	5.5
91.8	56.0	36.4	19.7
213.3	136.3	82.7	41.4
341.2	235.6	153.5	74.2
502.6	343.3	233.9	119.3
682.7	475.2	321.0	173.2
890.1	621.8	424.0	231.8
1120.0	784.7	540.4	294.9

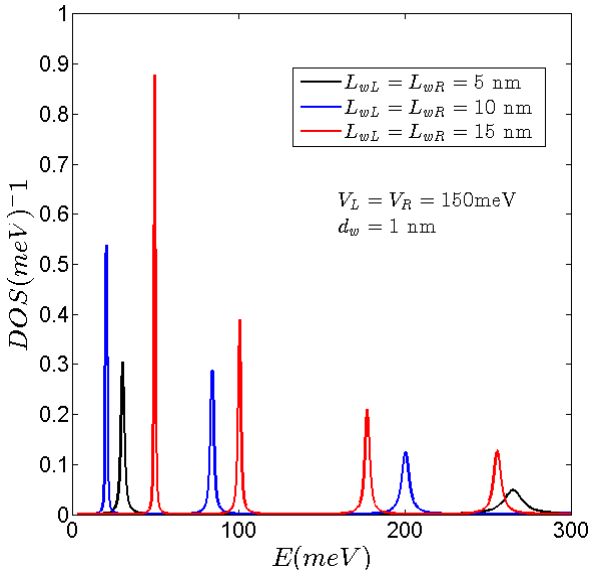

Fig. 4. DOS

4. CONCLUSION

Numerical results of the transmission coefficient are obtained for several parabolic double quantum well structures. We are found that the energy states and resonant peaks shift towards the lower energy region as the distance between wells increases. New resonant peaks emerge when the well widths or depths become wider. These structures are useful for the design of electronic devices.

References

[1] G. E. Gordon, "Cramming more components onto integrated circuits". Proceedings of the IEEE, 86, 1 (1998).
[2] S. Datta, Quantum Transport: Atom to transistor, Cambridge University Press, (2005).
[3] T. E. Lamas, A. A. Quivy, C. S. Sergio, G. M. Gusev, and J. C. Portal, J. Appl. Phys. 97, 076107 (2005)
[4] G. M. Gusev, A. A. Quivy, T. E. Lamas, J. R. Leite, A. K. Bakarov, A. I. Toropov, O. Estibals, and J. C. Portal, Phys. Rev. B 65, 205316 (2002).
[5] P. Pfeffer and W. Zawadzki, Phys. Rev. B 72, 035325 (2005).
[6] B. Vinter, C. Weisbuch, Quantum Semiconductor Structures, Academic Press, San Diego, (1991).
[7] P. Harrison, Quantum Wells, Wires and Dots: Theoretical and Computational Physics of Semiconductor Nanostructures, (3rd edt.) Wiley, (2010).
[8] K. H. Gao, G. Yu, Y. M. Zhou, W. Z. Zhou, T. Lin, J. H. Chu, N. Dai, A. J. Spring Thorpe, and D. G. Austing, J. Appl. Phys. 105, 013712 (2009).
[9] Parabolic Quantum Well (GaAs / AlAs) http://www.nextnano.com/nextnano3/tutorial/1Dtutorial_ParabolicQW.htm
[10] W. Chen, T.G. Andersson, Appl. Phys. Lett. 60, 1591 (1992).
[11] A. Wixforth, Surf. Sci. 305, 194 (1994).
[12] J. Gong, X-X.Liang and S.-L.Ban, Chinese Physics 14, 201 (2005).
[13] I. Rodriguez-Vargas,O. Y. Sanchez-Barbosa D. A. Contreras-Solorio and S. J. Vlaev, Progress In Electromagnetics Research Letters, 1, 237-243 (2008)
[14] L.Zhang, and H.-J. Xie, Phys. Rev. B, 68, 235315 (2003).
[15] G. M. Gusev, A. A. Quivy, T. E. Lamas, J. R. Leite, O. Estibals, J. C. Portal, Phys. Rev. B, 67, 155313 (2003).
[16] G. M. Gusev, A. A. Quivy, T. E. Lamas, J. R. Leite, O. Estibals and J. C. Portal, Physica E, 22, 336–340 (2004).
[17] A. L. Efros and E. I. Rashba, Phys. Rev. B, 73, 165325 (2006).
[18] R. C. Miller, A. C. Gossard, D. A. Kleinman, and O.Munteanu, Phys. Rev. B 29, 3740-3743 (1984).
[19] H. Cruz, and J. G. Muga, Phys. Rev. B 45, 11885 (1992).
[20] F. Capasso and R. A. Kiehl, J. Appl. Phys. 58, 1366 (1985).

Biographies

Mehmet BATI was born on March 01, 1984 in Midyat, Turkey. In 2001, he graduated the high school "Kemalpaşa Lisesi" in İzmir, in 2006, he graduated from Dokuz Eylül University with first-degree in faculty of art and science. He earned a master degree in Physics from the Erciyes University and a Ph.D. degree from the Dokuz Eylül University. He is married and has two children.

Research Article | Submit Manuscript

Turkish Journal of Materials

Influence of substrate type on morphology and photoluminescence properties of ZnO thin films prepared by ultrasonic spray pyrolysis method

Eda Bingöl[1], Fatih Bozali[1], Eyüp Fahri Keskenler[2], Vagif Nevruzoğlu[3], Murat Tomakin[1,*]

[1]Department of Physics, Recep Tayyip Erdogan University, Rize, Turkey,
[2]Department of Material Science and Nanotechnology Engineering, Recep Tayyip Erdogan University, Rize, Turkey,
[3]Department of Energy Systems Engineering, Recep Tayyip Erdogan University, Rize, Turkey,

Received: 24/09/2016; Accepted: 22/12/2016; Published: 31/12/2016
Turk. J. Mater. Vol: 1 No: 1 Page: 19-24 (2016)
SLOI: http://www.sloi.org/sloi-name-of-this-article
*Correspondence E-mail: murattomakin@yahoo.com

ABSTRACT In this study, ZnO thin films were grown on glass, n-Si (100), c axis textured graphite and indium tin oxide coated glass (ITO) substrates by ultrasonic spray pyrolysis method. X-ray diffraction studies showed that ZnO samples have hexagonal structure with (002) preferred direction. The preferred orientation of the sample prepared on ITO substrate changed from (002) to (101). Some diffraction peaks of graphite and ITO substrates were observed in X-ray diffraction pattern. Lattice parameters of ZnO samples grew on glass, graphite and ITO substrates were approximately equal to lattice parameters of bulk ZnO (a = 3.249 Å and c = 5.206 Å). Quasi-aligned hexagonal shaped ZnO microrods were obtained for glass and ITO substrates. Room temperature photoluminescence measurements indicated a sharp ultraviolet luminescence at ~380 nm. Band gap values were found from UV peak position between 3.25 – 3.28 eV. Relative intensity of defect related peaks between 400–700 nm in photoluminescence spectra decreased significantly for ITO substrate.

Keywords: ZnO; USP Method; Substrate; Format.

Cite this article: E. Bingöl, F. Bozali, E.F. Keskenler, V. Nevruzoğlu, M. Tomakin. Influence of substrate type on morphology and photoluminescence properties of ZnO thin films prepared by ultrasonic spray pyrolysis method. Turk. J. Mater. 1(1) (2016) 19-24.

1. INTRODUCTION

In recent years, micro- and nano-structured materials are becoming increasingly important in technology. These materials are intensively working for device applications such as field-effect transistors [1], single-electron transistors [2], photodiodes [3] and chemical sensor [4]. Among these materials ZnO has an important place due to its direct band gap of about 3.37 eV, its large exciton binding energy (60 meV) and its low cost. Therefore, fabrication of ZnO micro- and nano-structures in different morphologies is of critical importance for the development of novel device.

ZnO has various morphologies such as microsphere [5], microcomb [6], nanorod [7], nanotube [8] and nanowire [9]. Different methods such as chemical vapor deposition [10], thermal evaporation [11], spray pyrolysis [12] and chemical bath deposition [13] can be used for preparation of micro- and nano-structured ZnO samples. Spray pyrolysis method is simple and low cost for deposition of different materials [14]. Atomization of solution in spray method can be carry out by ultrasonic nebulizer, improved hydrolysis spraying, corona spraying, electrostatic spraying and pneumatic spraying [15]. Atomization type is important parameter due to better control over droplet size and its distribution on the substrate. Nowadays, spray by ultrasonic nebulizer has come into one of the most powerful methods for preparation of nanostructured materials [16]. Also, substrate type effects surface morphology of the thin films due to differences in the thermal conductivity and surface energy of the substrates [17].

In this study, undoped ZnO thin films were deposited on glass, Si, graphite and indium tin oxide coated glass substrates by ultrasonic spray pyrolysis (USP) method. Our aim is investigation of the correlation between structural and optical properties of ZnO thin films and substrates.

2. EXPERIMENTAL

ZnO thin films were prepared on different substrates (glass, n-Si (100), *c* axis textured graphite and indium tin oxide coated glass (ITO)) by ultrasonic spray pyrolysis in air atmosphere. First of all, substrates were cleaned ultrasonically with acetone, ethanol, and deionized water, respectively and then the substrates were dried by air flow. The initial solution was prepared from zinc chloride ($ZnCl_2$) at 0.15 M concentration in deionized water. Film growth was performed with a spray rate of about 2 ml/min. The substrate temperature was 400 °C and the process was carried out at atmospheric pressure. During growth, the substrates were rotated at 3.5 rpm in order to produce uniform and homogenous films. The crystal structure of ZnO thin films was examined by X-ray diffraction (XRD) using Rigaku Smartlab with CuK_α radiation (λ = 1.5408 Å) over the range 2θ = 30–60° at room temperature. Morphological information was obtained by JEOL JSM 6610 scanning electron microscope (SEM). Elemental analysis was studied by using Oxford Instruments Inca X-act energy dispersive X-ray spectroscopy (EDS) attached to the SEM. Room temperature photoluminescence (RTPL) spectra were measured using SpectraMax M5 spectrophotometer with a xenon flash lamp as light source operating at 280 nm and with an output power of 150 W.

3. RESULTS

Fig. 1 shows the XRD spectra of the ZnO thin films prepared on different substrates. ZnO thin films had hexagonal structure. The preferred orientation was (002) plane and its intensity were same approximately for glass and n-Si. The preferred orientation and peak intensity decreased for graphite and ITO substrates. Also, the preferred orientation changed from (002) plane to (101) plane for ITO substrate. A small diffraction peak at approximately 43° (+) was observed in XRD pattern of the ZnO thin films prepared on glass and n-Si substrates. This peak can be attributed from (200) plane of cubic ZnO phase (PDF Card No.: 01-077-9353). However, the orthorhombic Zn_2SiO_4 (zinc silicate) phase has (004) diffraction peak at approximately 43° (PDF Card No.: 00-024-1469). Zn_2SiO_4 phase can be formed due to relatively high deposition temperature of ZnO thin films. Similar results were found by another researcher for ZnO samples [18, 19]. Diffraction peaks of ITO (*) and graphite (#) structures were formed in the samples prepared on ITO and graphite substrates.

The lattice parameters *a* and *c* were calculated according to the following relation:

$$\frac{1}{d^2} = \frac{4}{3}\left(\frac{h^2+hk+k^2}{a^2}\right) + \frac{l^2}{c^2} \quad (1)$$

where *d* is interplanar spacing of atomic planes and (*hkl*) is Miller indices. Calculated latttices parameters were listed Table 1. Lattice parameters of ZnO samples for glass, graphite and ITO substrates were approximately equal to lattice parameters of bulk ZnO (*a* = 3.249 Å and *c* = 5.206 Å). But, large amount change in *a* and *c* values (3.271 Å and 5.238 Å) of ZnO thin film for n-Si substrate was observed.

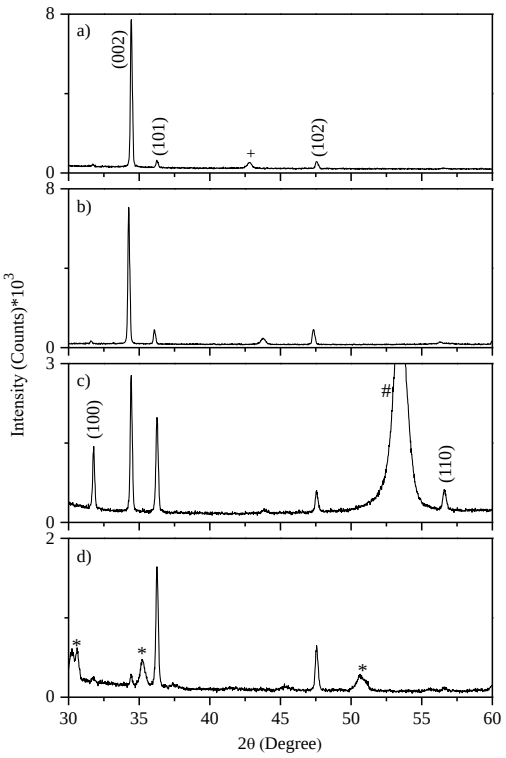

Figure 1. X-ray diffraction patterns of ZnO thin films for a) glass b) n-Si, c) graphite and d) ITO substrates.

Table 1. a and c attice parameters, compositional ratio, thickness (t) and band gap (Eg) of ZnO thin films.

Substrate	***a* (Å)**	***c* (Å)**	**Zn (at.%)**	**O (at.%)**	**Zn/O**	***t* (μm)**	**E_g (eV)**
Glass	3.256	5.213	51.2	48.8	1.05	1.20	3.26
n-Si	3.271	5.238	52.9	47.1	1.12	0.88	3.25
Graphite	3.254	5.214	52.4	47.6	1.10	0.56	3.27
ITO	3.253	5.211	54.8	45.2	1.21	0.55	3.28

The thickness of the films was determined from the cross-sectional SEM micrographs (Fig. 2.) and was listed in Table 1. The thickness of the ZnO thin films prepared on glass, n-Si, graphite and ITO substrate was found as 1.20 μm, 0.88 μm, 0.56 μm and 0.55 μm, respectively. It was observed that substrate type had significant effect on the thickness of ZnO samples and ZnO sample grown with the largest thickness on glass substrate. The surface morphologies of ZnO thin films were studied by SEM and results were shown in Fig. 2.

As can be seen, substrate type affects significantly surface morphology of the samples. This result can be attributed to the differences in the thermal conductivity and surface energy of the substrates [17]. The thermal conductivity and the surface energy values of the substrates were listed in Table 2. It can be seen from Table 2 that glass and ITO substrates have the lowest thermal conductivity value, and glass and n-Si substrates have the largest surface energy value. Samples prepared on glass and ITO grew as quasi-

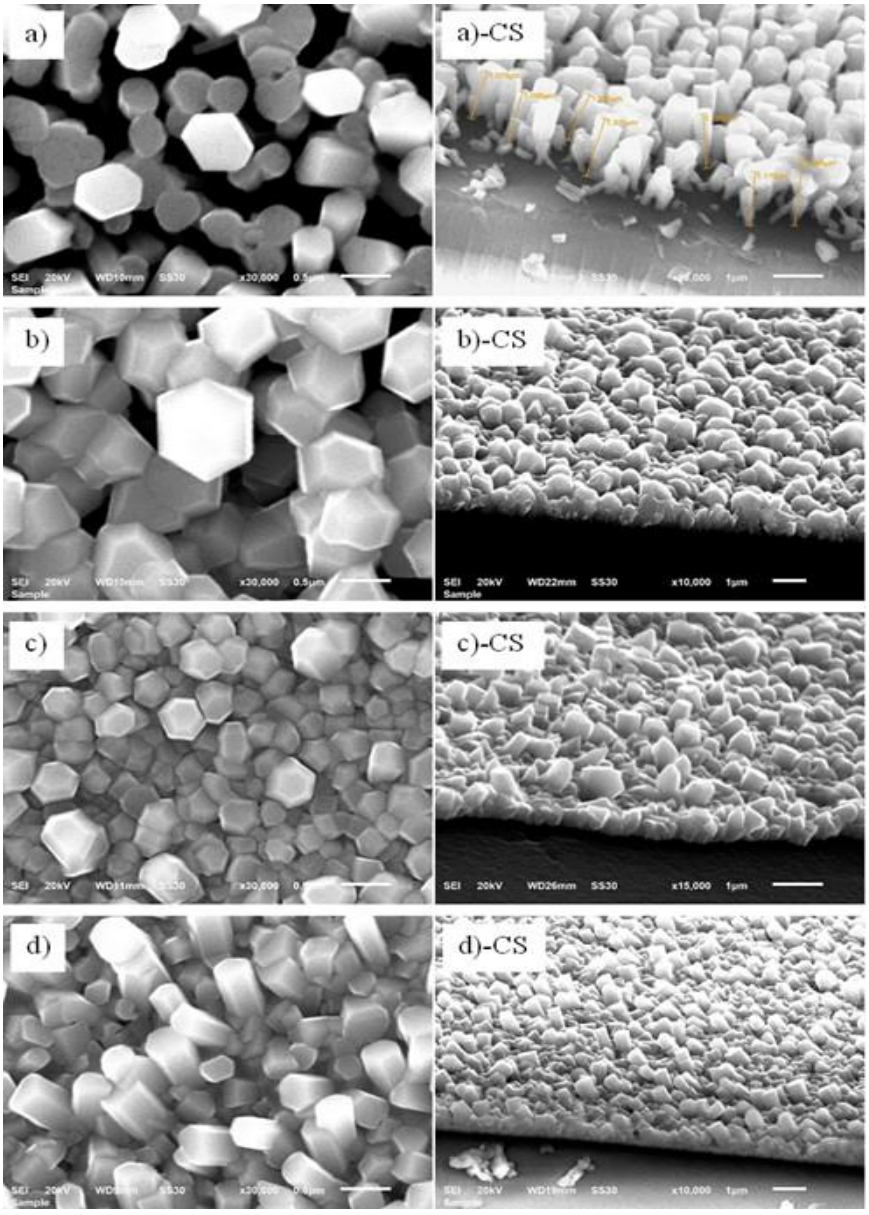

Figure 2. Surface and cross section (CS) scanning electron micrographs of ZnO thin films for a) glass b) n-Si, c) graphite and d) ITO substrates.

aligned hexagonal shaped microrods with diameters varying between 0.3 and 0.7 μm. It can be said according to these results that ZnO thin films prepared on substrates (glass and n-Si) with high surface energy have large thickness, and ZnO thin films prepared on substrates (glass and ITO) with low thermal conductivity have hexagonal shaped microrods. Different researchers were found similar hexagonal shaped microrods structure for ZnO thin films prepared with spray pyrolysis method [20-22]. However, while microrods for ZnO sample on glass substrate had c-axis orientation on substrate surface, microrods in ZnO thin film prepared on ITO had randomly orientation. The preferred orientation change seen in XRD data of the ZnO thin film prepared on ITO substrate confirms this result. The reason of randomly orientation in ZnO microrods prepared on ITO could be the lower surface energy of ITO than that of glass. The surface of the ZnO samples prepared on glass and n-Si had some voids. The larger grain size was obtained for n-Si substrate. Grain structure of ZnO thin film for graphite substrate was close packed, different size and shape. Zhang and co-worker in a similar study were obtained pyramidal-shaped nanosheets for ZnO prepared on graphite substrate [23]. The composition ratio of the films was determined by EDS analysis. Fig. 3 shows a typical EDS spectrum of the ZnO sample prepared on Si substrate. The atomic percent (at.%) of Zn and O in the films are listed in Table 1. It was observed that composition ratio of samples changed significantly depending on substrate type. All samples are Zn-rich because of Zn/O ratio is larger than 1. But ZnO sample prepared on glass substrate was more stoichiometric than the other samples.

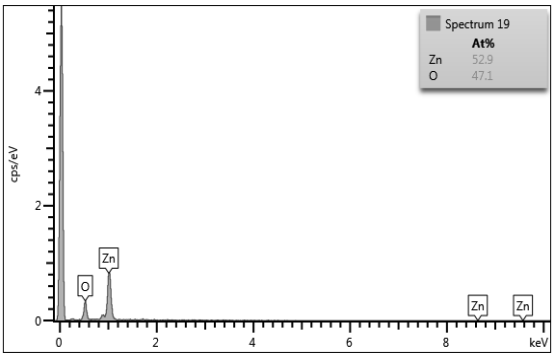

Figure 3. Energy dispersive X-ray spectroscopy of ZnO thin films for n-Si substrate.

Room temperature photoluminescence spectroscopy (RTPL) was performed for investigation of the optical properties and structural defects. Fig.4 shows RTPL spectra of the samples. The samples exhibited sharp and predominant UV luminescence at approximately 380 nm, which demonstrates high crystallinity. However, the intensity of UV peak for graphite and ITO substrate increased. The origin of near band edge UV emission is due to the free exciton recombination [24].

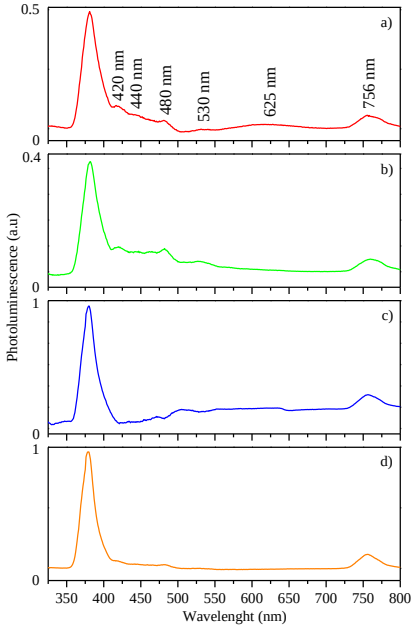

Figure 4. Room temperature photoluminescence spectra of the ZnO thin films for a) glass b) n-Si, c) graphite and d) ITO substrates.

The peak at 756 nm is related to second-order properties of the UV peak [25]. The position of UV peak was used for determining of band gap (E_g) of the samples. Obtained band gap values listed Table 1, which were between 3.25 – 3.28 eV. Five defect related peaks were observed at 420, 440, 480, 530 and 625 nm for RTPL spectra of ZnO samples on glass substrate. The peak at 420 nm attributes to interstitial zinc atoms (Zn_i) [21]. The peaks at 440 nm and 480 nm are related to transitions of interstitial Zn levels to vacancy Zn levels and transitions of interstitial O levels to vacancy O levels, respectively [26]. The peak at 530 nm can be related to vacancy Zn, interstitial Zn, vacancy O, interstitial O and anti-sites defects [25, 27]. The broad peak at 625 nm can be explain with to O and Zn anti-sites [28]. The defect peak at 625 nm for n-Si substrate and defects peaks between 400 – 500 nm for graphite substrate disappeared. In addition, the region between 400 – 700 nm in RTPL spectrum of ZnO on ITO substrate had become more flattened, which shows that defects concentrations decrease. We found that although ZnO thin films prepared on ITO and graphite substrate had lower XRD intensity, lower thickness and lower stoichiometry (higher Zn/O ratio), they had higher UV intensity, which is reverse in the expected situation. This result can be explained with surface properties of ZnO thin films. As can be seen from Fig. 2 ZnO thin films prepared on glass and n-Si substrates had more voids on their surface. Higher voids density increase surface defects and so UV intensity of ZnO thin films decrease. It is known that the effect of the surface becomes important when dealing with samples having high surface to volume ratio and so the presence of surface states must be considered as potential influencers on the material's optical properties [29].

Thus, substrate type affects significantly luminescence properties of the ZnO films by defect type and their concentration.

Table 2. Thermal conductivity and surface energy of glass, Si (100), graphite and ITO coated glass substrates [17, 30-33].

Substrate	Thermal conductivity (W/cmK)	Surface Energy (ergs/cm$^{2)}$
Glass	1.13×10^{-2}	2.0×10^{3}
n-Si	1.48	2.1×10^{3}
Graphite	16–20	70–80
ITO	3.20×10^{-2}	28–31

4. CONCLUSION

Structural and optical properties of ZnO thin films grown by ultrasonic spray pyrolysis on different substrates were investigated. It was determined from XRD result that ZnO samples have hexagonal structure. The preferred orientation of sample prepared on glass, n-Si and graphite substrates was (002) plane. But the preferred orientation for ITO substrate changed from (002) to (101). Also peak intensity decreased significantly for ITO and graphite substrates. The lattice parameters of *a* and *c* (3.271 Å and 5.238 Å) for ZnO thin film grown on n-Si substrate changed significantly compared to the bulk values (a = 3.249 Å and c = 5.206 Å). ZnO sample with the largest thickness was obtained on glass substrate. According to the SEM results, ZnO thin films prepared on glass and ITO substrates had a hexagonal rod morphology. But, ZnO microrods for ITO had randomly orientation on substrate surface. A sharp ultraviolet luminescence at 380 nm and some defects peaks at 420, 440, 480, 530 and 625 nm for all samples were observed from photoluminescence spectra. However, the maximum UV peak intensity was observed for ITO and graphite substrates.

Acknowledgement

This work was supported by the research fund of Recep Tayyip Erdogan University, Rize, Turkey, under Contract No. 2014.102.01.02.

References

[1] K.I. Chen, B.R. Li, Y.T. Chen, Silicon nanowire field-effect transistor-based biosensors for biomedical diagnosis and cellular recording investigation, Nano Today 6(2) (2011) 131-154.

[2] T.W. Kim, D.C. Choo, J.H. Shim, S.O. Kang, Single-electron transistors operating at room temperature, fabricated utilizing nanocrystals created by focused-ion beam, Appl Phys Lett 80(12) (2002) 2168-2170.

[3] H.T. Hsueh, S.J. Chang, F.Y. Hung, W.Y. Weng, C.L. Hsu, T.J. Hsueh, T.Y. Tsai, B.T. Dai, Fabrication of coaxial p-Cu2O/n-ZnO nanowire photodiodes, Superlattice Microst 49(5) (2011) 572-580.

[4] S. Paul, A. Helwig, G. Muller, F. Furtmayr, J. Teubert, M. Eickhoff, Opto-chemical sensor system for the detection of H-2 and hydrocarbons based on InGaN/GaN nanowires, Sensor Actuat B-Chem 173 (2012) 120-126.

[5] Y.X. Yan, Q. Liu, J. Wang, L.Y. Ji, X.Y. Jing, R.M. Li, L.H. Liu, Synthesis of ZnO hollow microspheres via an in-situ gas growth method, Powder Technol 232 (2012) 134-140.

[6] C. Li, G.J. Fang, F.H. Su, G.H. Li, X.G. Wu, X.Z. Zhao, Self-organized ZnO microcombs with cuboid nanobranches by simple thermal evaporation, Cryst Growth Des 6(11) (2006) 2588-2591.

[7] S.F. Wei, J.S. Lian, H. Wu, Annealing effect on the photoluminescence properties of ZnO nanorod array prepared by a PLD-assistant wet chemical method, Mater Charact 61(11) (2010) 1239-1244.

[8] Z.F. Liu, C.C. Liu, J. Ya, E. Lei, Controlled synthesis of ZnO and TiO2 nanotubes by chemical method and their application in dye-sensitized solar cells, Renew Energ 36(4) (2011) 1177-1181.

[9] O. Lupan, T. Pauporte, I.M. Tiginyanu, V.V. Ursaki, H. Heinrich, L. Chow, Optical properties of ZnO nanowire arrays electrodeposited on n- and p-type Si(1 1 1): Effects of thermal annealing, Mater Sci Eng B-Adv 176(16) (2011) 1277-1284.

[10] Z.J. Li, Z.F. Hu, F.J. Liu, J.A. Sun, H.Q. Huang, X.Q. Zhang, Y.S. Wang, High-quality hexagonal ZnO crystals grown by chemical vapor deposition, Mater Lett 65(5) (2011) 809-811.

[11] J.H. Zheng, Q. Jiang, J.S. Lian, Synthesis and optical properties of flower-like ZnO nanorods by thermal evaporation method, Appl Surf Sci 257(11) (2011) 5083-5087.

[12] T. Dedova, I.O. Acik, M. Krunks, V. Mikli, O. Volobujeva, A. Mere, Effect of substrate morphology on the nucleation and growth of ZnO nanorods prepared by spray pyrolysis, Thin Solid Films 520(14) (2012) 4650-4653.

[13] K.V. Gurav, U.M. Patil, S.M. Pawar, J.H. Kim, C.D. Lokhande, Controlled crystallite orientation in ZnO nanorods prepared by chemical bath deposition: Effect of H2O2, J Alloy Compd 509(29) (2011) 7723-7728.

[14] S.D. Shinde, G.E. Patil, D.D. Kajale, V.B. Gaikwad, G.H. Jain, Synthesis of ZnO nanorods by spray pyrolysis for H2S gas sensor, J Alloy Compd 528 (2012) 109-114.

[15] P.S. Patil, Versatility of chemical spray pyrolysis technique, Mater Chem Phys 59(3) (1999) 185-198.

[16] J.H. Bang, K.S. Suslick, Applications of Ultrasound to the Synthesis of Nanostructured Materials, Adv Mater 22(10) (2010) 1039-1059.

[17] G.H. Nam, S.H. Baek, I.K. Park, Growth of ZnO nanorods on graphite substrate and its application for Schottky diode, J Alloy Compd 613 (2014) 37-41.

[18] S. Yilmaz, E. Bacaksiz, I. Polat, Y. Atasoy, Fabrication and structural, electrical characterization of i-ZnO/n-ZnO nanorod homojunctions, Curr Appl Phys 12(5) (2012) 1326-1333.

[19] I. Polat, S. Yilmaz, I. Altin, E. Bacaksiz, M. Sokmen, The influence of Cu-doping on structural, optical and photocatalytic properties of ZnO nanorods, Mater Chem Phys 148(3) (2014) 528-532.

[20] U. Alver, T. Kilinc, E. Bacaksiz, S. Nezir, Temperature dependence of ZnO rods produced by ultrasonic spray pyrolysis method, Mater Chem Phys 106(2-3) (2007) 227-230.
[21] M. Tomakin, Structural and optical properties of ZnO and Al-doped ZnO microrods obtained by spray pyrolysis method using different solvents, Superlattice Microst 51(3) (2012) 372-380.
[22] S.J. Ikhmayies, Synthesis of ZnO Microrods by the Spray Pyrolysis Technique, J Electron Mater 45(8) (2016) 3964-3969.
[23] Z.K. Zhang, J.M. Bian, J.C. Sun, X.W. Ma, Y.X. Wang, C.H. Cheng, Y.M. Luo, H.Z. Liu, High optical quality ZnO films grown on graphite substrate for transferable optoelectronics devices by ultrasonic spray pyrolysis, Mater Res Bull 47(9) (2012) 2685-2688.
[24] Y.M. Hao, S.Y. Lou, S.M. Zhou, R.J. Yuan, G.Y. Zhu, N. Li, Structural, optical, and magnetic studies of manganese-doped zinc oxide hierarchical microspheres by self-assembly of nanoparticles, Nanoscale Res Lett 7 (2012) 1-9.
[25] F. Yi, Y.H. Huang, Z. Zhang, Q. Zhang, Y. Zhang, Photoluminescence and highly selective photoresponse of ZnO nanorod arrays, Opt Mater 35(8) (2013) 1532-1537.
[26] G. Srinet, R. Kumar, V. Sajal, Effects of aluminium doping on structural and photoluminescence properties of ZnO nanoparticles, Ceram Int 40(3) (2014) 4025-4031.
[27] G. Srinet, P. Varshney, R. Kumar, V. Sajal, P.K. Kulriya, M. Knobel, S.K. Sharma, Structural, optical and magnetic properties of Zn-1 (-) xCoxO prepared by the sol-gel route, Ceram Int 39(6) (2013) 6077-6085.
[28] R.S. Zeferino, M.B. Flores, U. Pal, Photoluminescence and Raman Scattering in Ag-doped ZnO Nanoparticles, J Appl Phys 109(1) (2011).
[29] J. Rodrigues, T. Holz, R. FathAllah, D. Gonzalez, T. Ben, M.R. Correia, T. Monteiro, F.M. Costa, Effect of N2 and H2 plasma treatments on band edge emission of ZnO microrods, Sci Rep 5, 10783 (2015) 1–9.
[30] Kui-Xiang Ma, U, Chee-Hin Ho, Furong Zhu, Tai-Shung Chung, Investigation of surface energy for organic light emitting polymers and indium tin oxide, Thin Solid Films 371 (2000) 140–147.
[31] T. Yagi, K.Tamano, Y. Sato, N. Taketoshi, T. Baba, Y. Shigesato, Analysis on thermal properties of tin doped indium oxide films by picosecond thermoreflectance measurement, J Vac Sci Technol A 23 (2005) 1180–1186.
[32] U. Hammerschmidt, M. Abid, The thermal conductivity of glass-sieves: I. Liquid saturated frits, International J Thermal Sciences 96 (2015) 119–127.
[33] B. Lawn, Fracture of brittle solids, Cambridge University Press, Second edition (1993).